The Dark Energy Survey Science Program

Abstract

The Dark Energy Survey (DES) will enable measurements of the dark energy and dark matter densities and the dark energy equation of state through four independent methods: galaxy clusters, weak gravitational lensing, galaxy angular clustering (baryon acoustic oscillations), and supernovae. These methods, highlighted by the Dark Energy Task Force Report (DETF) as the most promising, are doubly complementary: they constrain different combinations of cosmological model parameters and are subject to different systematic errors. By exploiting this multiplicity, the DES will make a substantial and robust advance in the precision of dark energy measurements at the level envisioned for a DETF Stage III (*i.e.*, near-term, intermediate-scale) experiment. It will also explore and develop methods to mitigate the systematic errors for the different dark energy methods.

This description of the Dark Energy Science Program, originally written as part of the DES proposal to NSF and DOE in December 2006, is organized as follows. We first present the forecast constraints on dark energy parameters; we then summarize each of the four proposed techniques for probing dark energy, describe how they will be implemented in DES, detail the primary systematic errors and how we plan to control them, list the assumptions underlying the parameter forecasts, and briefly mention ancillary science that can be done with each method. After describing other dark energy probes that DES will enable, we describe an extensive program of numerical simulations that will be used to nail down key theoretical undecertainties and that will serve as a testbed for developing DES analysis tools. We end by summarizing the photometric redshift (photo-z) estimates that are central to the entire DES science program.

1. Survey Parameters & Forecast Dark Energy Constraints

The DES comprises two multi-band imaging surveys, a wide-field survey and a narrow time-domain survey. The wide-field survey covers 5000 sq. deg. in the south Galactic cap, completely encompassing the 4000 sq. deg. area of the South Pole Telescope (SPT) Sunyaev-Zel'dovich effect (SZE) survey (Ruhl et al. 2004), reaching $\sim$ 24th magnitude in SDSS $griz$ filters. The depth and filter coverage of the wide-field survey are chosen primarily to achieve accurate galaxy and cluster photo-z measurements to redshifts $z \gtrsim 1$ (§8.). The wide-field survey will detect over 100,000 galaxy clusters and will measure shapes, photo-z's, and positions for $\sim$ 300 million galaxies. Upon formal approval by ESO of the near-infrared Vista Hemisphere Survey covering the DES area in J, H, and K filters, we plan to add Y-band to the fiducial filter set for the wide-field DES (the Y-band filter for DECam will be purchased by the DES consortium). The combined $grizYJHK$ data will extend the range of precise galaxy photo-z's to $z \sim 2$. However, all our forecasts rely on photo-z error estimates based on simulations of DES $griz$ data alone.

The DES Supernova (SN) Survey involves frequent, repeat imaging of a much smaller area of sky to discover and measure large numbers of supernova light curves; the current baseline SN survey (§4.) features deep imaging in riz filters over 9 sq. deg. with a cadence of 5 visits per lunation, yielding good-quality light curves for over 1000 type Ia supernovae to redshift $z \sim 1$. The SN survey is expected to use up to $\sim$ 10% of the available photometric time for DES, plus a larger fraction of the useable, non-photometric time.

In forecasting dark energy parameter constraints for DES, we follow the approach of the DETF. We parametrize the redshift evolution of the dark energy equation of state by $w(a) = w_0 + w_a(1-a)$, where $a(t) = 1/(1+z)$ is the cosmic scale factor. In order to compare dark energy methods and projects, the DETF defined a figure of merit (FoM) that is proportional to the reciprocal of the area in the $w_0 - w_a$ plane that encloses the 95% CL region. Defining a pivot epoch, a_p, at which the uncertainty in $w(a)$ is minimized for a given experiment, the DETF FoM is $[\sigma(w_p)\sigma(w_a)]^{-1}$.

The DETF provided an estimate for the Stage II FoM, where Stage II includes projections from on-going surveys as well as the forecast statistical precision of Planck CMB measurements on cosmological parameters. The DETF also provided optimistic and pessimistic forecasts for the FoM for 'generic' Stage III and Stage IV projects exploiting the four dark energy techniques, where optimistic (pessimistic) means the assumed systematic errors are small (not small) compared to the statistical errors. They found that a Stage III imaging experiment combining the four techniques and modeled closely on DES, in combination with SZE cluster detections modeled closely on SPT, should achieve an increase in the FoM of a factor of

3 to 5 relative to Stage II, depending on the level of optimism. Our own forecast constraints for DES are given below in Table 1 and correspond to an increase by a factor of 4.6 in the combined FoM over the DETF Stage II value. Our projections for the FoM for each method lie toward the optimistic ends of the DETF projections for Stage III; we justify the assumptions underlying these projections in §2.-5..

We note that considerable uncertainties in the systematic error levels remain for each of the methods. Some of those will be pinned down by further theoretical work, *e.g.*, via N-body simulations, while others will likely only be determined once we have the large DES data set in hand and carry out internal and external cross checks of each method. On the other hand, we find that the forecast combined FoM for DES appears to be robust to changing the level of systematic uncertainty in any one of the dark energy probes.

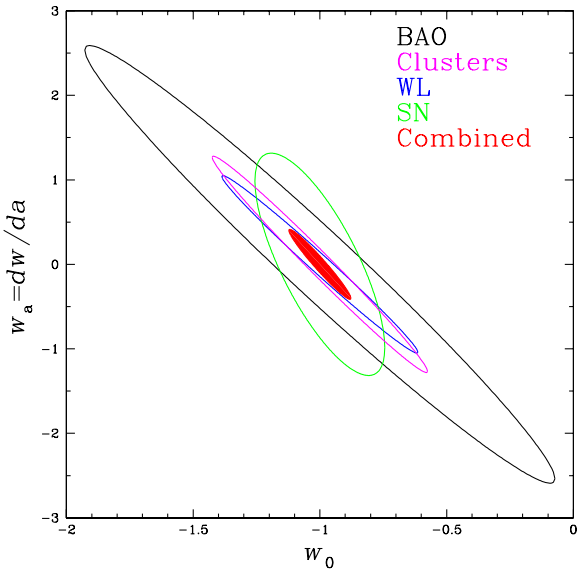

Figure 1: 68% CL forecast DES constraints in the w_0–w_a plane from the four probes: BAO (black), clusters (magenta), weak lensing (blue), and SNe (green), each combined with the Planck CMB prior; the filled, red region shows the constraints from combining the four methods. All other cosmological parameters and the nuisance parameters for each method have been marginalized. To better show the degeneracies for each method, in this plot we have *not* included the DETF stage II constraints, unlike in Table 1.

Our forecasts are based on Fisher matrix calculations. For the fiducial cosmological model, we take the matter density $\Omega_m h^2 = 0.14$, dark energy density $\Omega_{DE} = 0.73$, $w_0 = -1$, $w_a = 0$, matter power spectrum amplitude $\sigma_8 = 0.75$, baryon density $\Omega_b h^2 = 0.024$, spectral index $n_s = 1$, and spatial curvature $\Omega_k = 0$, consistent with current WMAP constraints. We allow each of these parameters, including the spatial curvature, to vary, but we impose massless neutrinos, no tensor contribution to the CMB, and no running of the scalar spectral index. We assume that the primordial perturbations are adiabatic and Gaussian, as expected in the simplest classes of inflation models. The forecasts assume a Planck prior for the CMB, as adopted by the DETF. For each dark energy probe, we derive marginalized 68% CL constraints on w_0 and w_a using the Planck prior and the survey parameters and assumptions outlined in the following sections. We then combine the Fisher matrices for all four probes to derive the combined marginalized constraints. The results are shown in Fig. 1 and displayed in Table 1.

In addition to measuring the effective dark energy equation of state and determining whether it is consistent with Einstein's cosmological constant, we plan to address the fundamental question of whether cosmic acceleration is caused by dark energy or by a modification of General Relativity (GR) on large scales. Such a modification is expected to alter the growth rate of large-scale structure in a manner not captured by a single

Method	$\sigma(\Omega_{DE})$	$\sigma(w_0)$	$\sigma(w_a)$	z_p	$\sigma(w_p)$	$[\sigma(w_a)\sigma(w_p)]^{-1}$
BAO	0.010	0.097	0.408	0.29	0.034	72.8
Clusters	0.006	0.083	0.287	0.38	0.023	152.4
Weak Lensing	0.007	0.077	0.252	0.40	0.025	155.8
Supernovae	0.008	0.094	0.401	0.29	0.023	107.5
Combined DES	0.004	0.061	0.217	0.37	0.018	263.7
DETF Stage II Combined	0.012	0.112	0.498	0.27	0.035	57.9

Table 1: 68% CL marginalized forecast errorbars for the 4 DES probes on the dark energy density and equation of state parameters, in each case including Planck priors *and* the DETF Stage II constraints. The last column is the DETF FoM; z_p is the pivot redshift. Stage II constraints used here agree with those in the DETF report to better than 10%.

equation of state function $w(a)$. The four techniques in DES employ different combinations of geometric and structure-growth based probes, so that comparisons of the results will enable us to constrain departures from GR.

2. Galaxy Clusters

Massive structures observed in the Universe today bear the marks of three influences: the spectrum of initial density perturbations, the physics of gravitational collapse, and the dynamically evolving underlying metric. Galaxy clusters, the largest virialized objects in the mass distribution, are a particularly tractable target for observations of structure and its evolution over cosmic time. For any set of cosmological parameters, the growth of cluster-sized dark matter haloes as a function of redshift and mass can be precisely predicted from N-body simulations. Comparing these predictions to observations of the real universe provides constraints on cosmology (Allen et al. 2003; Bahcall et al. 2003; Gladders et al. 2007). Large cluster surveys that extend to intermediate or high redshift can in principle provide very precise measurements of the cosmic expansion history, thereby revealing the nature of dark energy (e.g. Wang & Steinhardt 1998; Haiman et al. 2001).

A basic example of one such comparison is the redshift distribution of clusters in a survey that finds systems of mass M with efficiency $f(M,z)$ at redshift z:

$$\frac{d^2N(z)}{dzd\Omega} = \frac{c}{H(z)} D_A^2 (1+z)^2 \int_0^\infty f(M,z) \frac{dn(z)}{dM} dM \ , \tag{1}$$

where $dn(z)/dM$ is the space density of clusters of mass M in comoving coordinates, $H(z)$ is the Hubble parameter as a function of redshift, and $D_A(z)$ is the angular diameter distance. In an ideal case, the detection probability $f(M,z)$ is approximately a step function with a $z-$dependent mass threshold $M_{\rm min}(z)$.

The cosmological sensitivity of cluster counts arises from two factors:

- Geometry: The volume per unit solid angle and redshift depends sensitively on cosmological parameters.
- Abundance Evolution: The evolution of the number density of clusters, $dn(z)/dM$, depends on the growth rate of density perturbations, which is determined by the expansion rate $H(z)$ and thereby the cosmological parameters.

The cluster counting method depends critically on understanding the mapping between confidently predicted properties such as halo mass and the observed properties of clusters, such as galaxy content, X-ray emission, Sunyaev-Zeldovich flux decrement, or weak lensing shear. In fact, cosmological sensitivity also arises here, because the observed flux of a cluster at a particular redshift maps into a luminosity and mass

that depends on the distance to that redshift. In Eqn. 1, this mapping is approximated by a mass dependent selection function, $f(M,z)$. In fact, the selection is more directly dependent on some cluster observable, O, and the observed number function can be rewritten:

$$\frac{d^2N(z)}{dzd\Omega} = \frac{c}{H(z)} D_A^2 (1+z)^2 \int_{O_{min}}^{\infty} f(O,z) dO \int_0^{\infty} g(O|M,z) \frac{dn(z)}{dM} dM \ . \quad (2)$$

This mapping includes both a selection function more precisely expressed in observable space, $f(O,z)$, and a probabilistic mass-observable relation, $g(O|M,z)$. The selection function $f(O,z)$ is largely determined by observational issues, while the intrinsic mass-observable relation $g(O|M,z)$ contains important information about cluster physics.

2.1 Galaxy Clusters in DES

The Dark Energy Survey will provide a superb data set for cluster cosmology, a substantial advance beyond the largest on-going optical imaging surveys such as the SDSS and RCS-II. The DES will cover over half the sky area of the SDSS (York et al. 2000) but with about three times the redshift reach. It will cover four times the area of the RCS-II with four optical passbands instead of three. Based on current survey results and on numerical simulations populated with galaxies with observed properties (see §7.3), for the fiducial cosmology we expect to optically detect $\sim 170,000$ clusters with > 10 bright red-sequence galaxies and with masses greater than $\sim 5 \times 10^{13} M_\odot$ out to $z \sim 1.5$; the number of lower-richness groups detected will be even larger. The predicted redshift distribution for optically selected DES clusters above this limit is shown as the upper curve in the right panel of Figure 2.

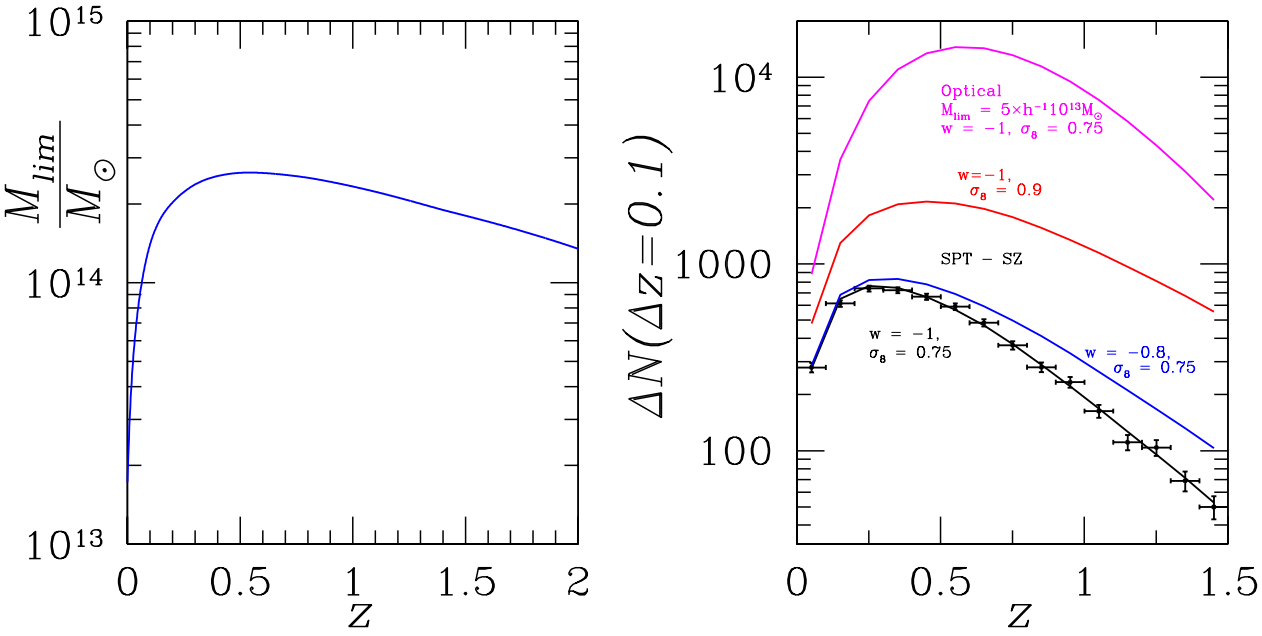

Figure 2: *Left panel:* Predicted SPT-SZE 4σ cluster mass detection threshold as a function of redshift (see §2.3); for optical cluster detection by DES, the mass limit is typically a factor of ~ 4 lower over most of this redshift range. *Right panel:* Expected cluster number counts (for $w = -1$) as a function of redshift for the approximate mass limits for DES optical cluster detection (purple) and for SPT-SZE detection for $\sigma_8 = 0.75$ (black) and 0.9 (red); for comparison the SPT SZE cluster counts for $w = -0.8$ and $\sigma_8 = 0.75$ are shown in blue, showing the sensitivity to w.

The red-sequence optical cluster detection method is now mature, with many tens of thousands of clusters already detected and characterized (Koester et al. 2007). It has already been applied across the full DES redshift range (Gladders et al. 2007), albeit over much smaller sky area, and the red-sequence galaxies on which the method relies have been shown to be ubiquitous in clusters throughout the redshift range of interest for DES. The number of bright galaxies in a cluster (the richness) and their total luminosity can be determined using statistical background subtraction and used as observable proxies for cluster mass (e.g. Lin, Mohr, & Stanford 2003; Yee & Ellingson 2003). The spectral energy distributions of red-sequence cluster galaxies are simple and homogeneous, enabling demonstrated measurement of cluster photometric redshifts with $\Delta z \lesssim 0.02$ and often $\lesssim 0.01$, consistent with the predicted precision for DES (see §8.2).

A critical feature of the DES is its ability to *directly* calibrate the mean mass-observable relation and its evolution using weak lensing (see §2.2). This direct mass calibration is essential for achieving precise and robust cluster dark energy constraints. We note that it cannot be delivered with a narrow-field imager that just targets the cores of clusters discovered, e.g., by the Sunyaev-Zel'dovich effect, in order to estimate their photometric redshifts.

A unique feature of the DES cluster survey is its complete overlap with the South Pole Telescope (SPT) survey region. The SPT (Ruhl et al. 2004) will identify clusters based on their integrated Sunyaev-Zel'dovich (SZE) (SZE Sunyaev & Zel'dovich 1970) flux decrement, which is expected to be tightly (at about the 10 % level) and robustly correlated with cluster mass (see §7.2). The 4σ SZE threshold for SPT corresponds to a nearly redshift-independent cluster mass threshold of $M \approx 2 \times 10^{14} M_{\odot}$ (see Fig. 2 and §2.3). Because clusters of this mass contain > 30 luminous red galaxies in the central Mpc, DES will independently detect and provide accurate photometric redshift estimates for essentially every SPT cluster out to $z \sim 1.3$ (and beyond, in combination with VHS; see §8.) and provide independent weak lensing calibration of the SZE flux-mass relation. Together, the DES and SPT offer unique advantages to precision cluster cosmology; the interested DES and SPT scientists will form a joint working group to carry forward this analysis.

2.2 Cluster Systematic Uncertainties

To probe dark energy with clusters, we must have precise theoretical predictions for the halo mass function, $dn(z)/dM$, as well as controlled understanding of the mass-observable relation, $g(O|M,z)$, and the selection function, $f(O,z)$. The theoretical uncertainty in the mass function is currently at the $\sim 10\%$ level (e.g. Warren et al. 2006); the program of simulations described in §7. aims to bring that down by a factor of several, ensuring that it will be a negligible part of the cluster cosmology error budget. The main systematic concern for cluster cosmology is therefore determining the mass-observable relations and, to a lesser extent, the observable selection functions. Inferring cosmological parameters from the observed distributions of cluster properties, either SZE or optical, requires knowledge of the form, scatter, and redshift evolution of these distributions. Here we describe three interlocking strategies that we will pursue to obtain them.

Direct Theoretical Prediction:

The first approach involves refining theoretical predictions, in concert with information gleaned from precursor surveys. §7.2 describes a program of N-body+hydro simulations aimed at improved modeling of the relation between SZE flux and cluster mass, the scatter therein, and its dependence on cluster gas physics, including redshift-dependent feedback from SNe, AGN, etc. Precursor SZE surveys now in progress, such as SZA, AMI, and APEX, will provide high-resolution SZE maps to test these predictions. An important goal of the simulation program will be to test and refine the parameterized forms of the mass-observable and survey selection functions assumed in cluster dark energy forecasts (§2.3). In addition, the simulations will be used to examine the relationships between the scatter in the mass-observable relation and variations in the amount of unvirialized cluster substructure (O'Hara et al. 2006). If clusters can be partitioned based on some morphological structure measure, then we may be able to devise improved analysis techniques that capitalize on the smaller-scatter subsamples.

This approach may be particularly fruitful for the optically identified DES clusters, because the sample is very large and the scatter in the optical richness-mass relation is larger than that between SZE flux and mass (Gladders et al. 2007; Benson et al. 2004). Direct theoretical prediction of the optical properties of clusters is the subject of intense effort (see §7.); the complexity of galaxy formation physics makes this a challenge, but real progress is being made. For example, Conroy et al. (2006) provide a method for connecting detailed spectroscopic observations of galaxies with N-body simulations in order to predict, e.g., the optical observables of clusters. The DES simulation group is producing a sequence of increasingly realistic mock catalogs that are being subject to red-sequence cluster finding analyses. These will help determine the DES optical selection function $f(O,z)$ and enable realistic assessment of the impact of line-of-sight blending on optical richness estimation. These methods are also being extensively tested using precursor surveys such as the SDSS, RCS-II, and the Blanco Cosmology Survey.

Self Calibration:

A powerful technique for handling the cluster mass scaling relations takes advantage of the additional information and therefore the cross checks that cluster samples provide, a technique known as self-calibration (Majumdar & Mohr 2003, 2004; Hu 2003; Lima & Hu 2004, 2005). The shape and amplitude of the cluster abundance function, $dn/dOdz$ (as opposed to its integral above a threshold), and the cluster spatial correlations as a function of observable and redshift are additional measureable quantities that must all simultaneously match the theoretical predictions. These quantities depend on the selection function $f(O,z)$ and the mass-observable relation $g(O|M,z)$ in different ways. Demanding consistency among the various measurements provides internal constraints on the mass-observable relation and the selection function, substantially tightening the cosmological constraints from clusters. Moreover, this technique allows for external mass calibration information such as that from weak lensing, galaxy velocity dispersions, or hydrostatic masses to be folded into the analysis self-consistently. In particular, by parametrizing the mass–observable relation the residual uncertainties in the cluster masses are directly reflected through weakened cosmological constraints. Recent work using the RCS-1 optical cluster sample (Gladders et al. 2007) demonstrates that such self-calibration approaches are viable in practice.

Direct Calibration with Weak Lensing:

DES data will allow direct measurement of the mean mass-observable relations and their evolution, $\langle M\rangle(O,z)$, through statistical weak gravitational lensing (e.g. Metzler et al. 2001; Dodelson 2004; Sealfon et al. 2006). Johnston et al. (2007a) have shown via direct analysis of N-body simulations that statistical weak lensing measures of the cluster-shear correlation function can be inverted in a model-independent way to provide unbiased estimates of the average 3D mass profile and virial mass for a sample of clusters, with an accuracy of a few %. As shown in Fig. 3, application of this technique to SDSS data has shown that both the mean cluster virial radius r_{200} and the virial mass can be inferred directly. DES cluster samples will be large enough to allow measurement of the mean cluster mass profile in a number of independent bins in both cluster observable, e.g., optical richness or SZE decrement, and redshift. In practice, the accuracy of these lensing-derived mean mass profiles depends upon the quality of the photometric redshifts for source galaxies (§8.), and the ability to precisely determine the shear (§3.); application to and tests on SDSS clusters have shown that these do not appear to be major limiting factors (Sheldon et al. 2007).

Because the lensing mass calibration derives from measurement of the cluster-shear correlation function, it is not biased by the projection of *uncorrelated* mass along the line of sight, a significant systematic effect for *individual* cluster weak lensing mass estimates or for shear-selected cluster samples. Moreover, as Fig. 3 shows, the effect of *correlated* mass along the line of sight appears to be quite small within the virial radius, for the rich clusters of primary interest for DES. Because the cluster counting dark energy probe depends critically on accurate statistical mass estimation, we emphasize how powerful it is to have this independent cross check.

Finally, we expect to develop a program of spectroscopic follow-up of a subsample of DES-SPT clusters. Multi-fiber spectroscopy should enable us to determine velocity dispersions for these clusters, thereby pro-

viding dynamical mass estimates and possible additional constraints on the scatter in the mass-observable relation.

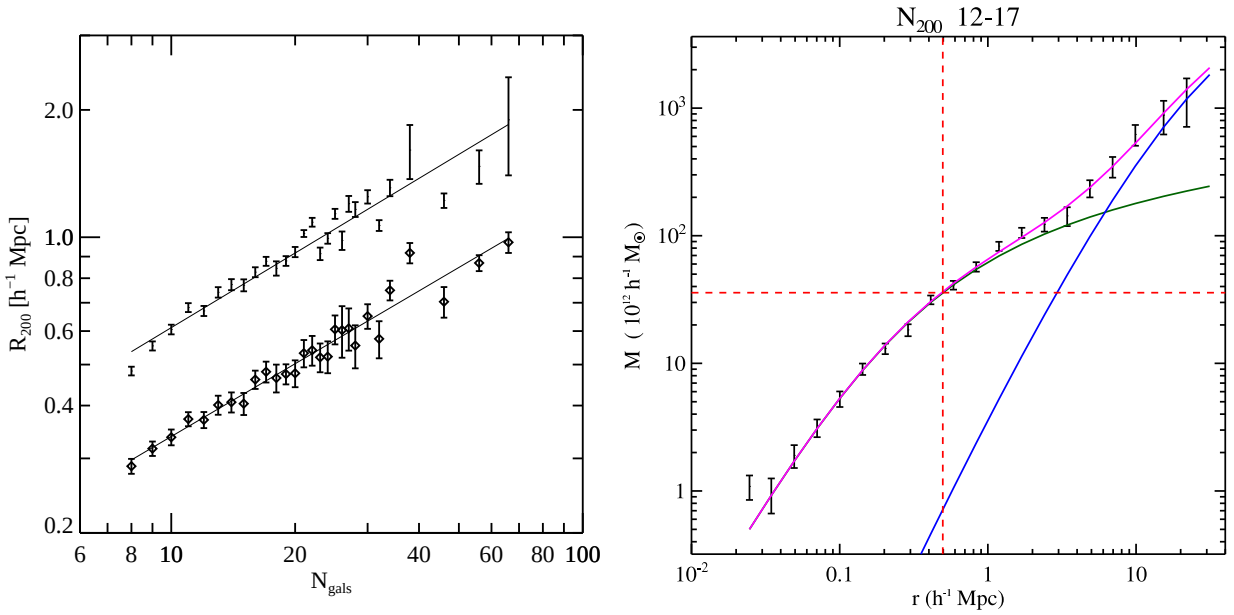

Figure 3: Mean measured properties of SDSS clusters. *Left panel:* mean radius at which the galaxy density is 666 (diamonds) or 200 (bars) times the mean galaxy density, as a function of optical cluster richness, N_{gals} (Hansen et al. 2005). *Right panel:* mean cluster 3d mass profile inferred from weak lensing cluster-shear measurements for clusters identified optically and containing $12 < N_{gals} < 17$ galaxies brighter than $L^*/2$ along the red cluster sequence (Sheldon et al 2007, Johnston et al 2007b); dashed red lines denote the virial radius and virial mass, green curve shows the best-fit NFW profile for the points inside the virial radius, blue line indicates expected contribution from projected mass correlated with the cluster (the two-halo term in halo model parlance), and purple curve shows the model sum; innermost bin shows contribution from the central galaxy.

In addition to these multiple approaches to constraining the mass-observable relation, we will also pursue multiple methods for testing the cluster selection function, $f(O, z)$, which we outline briefly here.

The Optical Selection Function:

As noted above, massive clusters contain large numbers of luminous red galaxies within their cores and are therefore straightforward to detect with red-sequence methods that have been developed for on-going surveys. While we are working to further optimize such methods, we note that the purity and completeness for red-sequence cluster-selected catalogs, estimated from realistic mock catalogs and from intercomparison of detection methods, are both greater than 90% for masses above $10^{14} M_{\odot}$ in the SDSS (Koester et al. 2007); analysis of simulated catalogs for DES indicates a similar level of expected performance. The effects of line-of-sight projection become more important at high redshift, altering the mass-observable relation $g(O|M, z)$, but this effect can be quantified with simulations (§7.) and in any case has little effect on the ability to detect a cluster which contains 10 or more red-sequence galaxies.

SZE Selection Function:

Cluster SZE selection using multiple mm-wave frequencies with arcminute angular resolution such as that delivered by the SPT is expected to be quite clean, because the cluster signal differs from the primary CMB anisotropy both in angular scale and spectrum. Complications in the selection of clusters from the SPT SZE survey are expected primarily from line-of-sight projection and from radio point source contamination

of SZE flux measurements (Vale & White 2006). Much work is currently underway to understand these issues in greater detail (e.g., Schulz and White 2003; White and Majumdar 2004; Melin, Bartlett, and Delabrouille 2005). The two most uncertain effects are radio-loud AGN, potentially associated with the clusters themselves, and sub-mm bright galaxies, high-redshift galaxies either undergoing bursts of star formation or harboring an AGN but in either case enshrouded by dust (White and Majumdar 2004). Multi-frequency observations such as those planned for SPT can alleviate this problem. These contaminants will also be better understood by a program of optical identification of clusters in small-area, high-resolution precursor SZE surveys that are underway, e.g., with the SZA and AMI, as well as through study of the relationship between existing radio surveys (e.g., FIRST, NVSS) and large cluster catalogs selected in the optical or X-ray (Lin & Mohr 2007).

Cross-checks of Selection Functions:

While mock catalogs derived from simulations will tell us much about the cluster selection function, crucial tests of completeness will come from comparison of the optical and SZE derived cluster catalogs from DES, SPT, and other SZE experiments such as APEX and ACT that will survey within the DES survey footprint. Since DES optical cluster selection extends well below the SPT mass threshold over this redshift range (Fig. 2), it will provide an important cross-check on the SPT SZE selection function, offering a way to mitigate the effects of radio galaxies in SZE selection. By the same token, SZE cluster detection can provide a check on the effects of projected large-scale structure on optical cluster selection noted above. Additional tests of cluster selection that we will explore include shear selection of clusters in DES (Hennawi & Spergel 2005; Wittman et al. 2006) and X-ray selection through existing XMM and Chandra observations within the DES and SPT survey regions. Although shear selection suffers from complex projection effects, a relatively high mass threshold, and relatively narrow range of redshift sensitivity, a subset of high-mass, shear-selected clusters will provide a unique test of the completeness of cluster samples selected from stellar or gaseous baryon content. X–ray cluster selection has been employed for over two decades and is still responsible for the bulk of the confirmed clusters at redshifts $z > 0.2$. In coordination with the 100 deg^2 Blanco Cosmology Survey, a dedicated XMM survey program (PI Boehringer) is just beginning and, together with serendipitous XMM and Chandra pointings within the DES and SPT region, will provide the data required for a detailed comparison of X-ray, SZE, optical, and shear cluster selection. Results from these ongoing precursor surveys will inform the analysis of the DES cluster survey cosmology program.

2.3 Cluster Forecasts

While dark energy constraints can in principle be obtained from optically selected clusters in the DES alone, as noted above inclusion of the SPT data allows cross-checking of systematic uncertainties, use of an observable—the Sunyaev-Zel'dovich effect flux decrement—that correlates tightly with cluster mass, and investigation of relations among the gas, galaxy, and dark matter contents of clusters. Therefore, in §1., we present only dark energy constraints expected from the combined DES+SPT samples.

We predict the SPT SZE mass threshold and detected cluster population using conservative estimates of SPT performance. These include a $\theta_{FWHM} = 1'$ beam, one channel at 150 GHz, and a 4σ detection threshold corresponding to a limiting flux of $S_\nu = 1.52$ mJy. To account for clusters larger than the beam size, we allow beam degradation (combining pixels) up to 20 arcmin (Battye & Weller 2003); we neglect CMB and point source confusion noise. The cluster SZE mass-observable relation is parametrized as a power-law relation that evolves as $A_0(1+z)^\gamma$. This relation is assumed to have an unknown log-normal scatter, and the redshift evolution of the variance is taken to be linear, $\sigma^2_{SZE-M}(z) = \sigma_0^2 + \sigma_1^2 z$. Together this yields a 4-parameter model for the SZE mass–observable relation $g(O|M,z)$. The mass-observable relation is constrained by employing three mass bins within redshift bins of $\Delta z = 0.1$ and assuming 30% accurate weak lensing cluster mass calibration for individual clusters in each bin. A more accurate treatment of weak lensing mass reconstruction assuming NFW mass profiles and the expected redshift distribution of DES source galaxies yields fractional lensing mass errors as a function of cluster mass and redshift that are

somewhat larger but within a factor of two of this approximation. Galaxy cluster clustering was used only through the variance of cluster counts within 10 deg^2 cells, which provides a constraint on the cluster bias and therefore the cluster masses. The lensing and clustering information provide priors on the parameters in $g(O|M,z)$; these 'nuisance' parameters are marginalized over, along with other cosmological parameters, in deriving the cluster constraints shown in Fig. 1.

For the fiducial ΛCDM ($w = -1$) cosmology, the assumptions above give the cluster SZE mass limit and abundance function shown in Fig. 2. For the constraints shown in Fig. 1, we use a maximum cluster redshift $z_{max} = 1.5$. For $\sigma_8 = 0.75, 0.8$, and 0.9, we find $\approx 5,600$, $9,200$, and $21,000$ SPT SZE clusters at 4σ respectively over this redshift range, showing a very strong sensitivity of the cluster counts to the power spectrum normalization. However, Fig. 2 shows that the dependence of the cluster abundance on redshift allows one to separate the effects of σ_8 and the dark energy equation of state w. For the forecast shown in Fig. 1, we conservatively use the low value of the power spectrum normalization, $\sigma_8 = 0.75$, recently reported by WMAP (Spergel et al. 2007), although reanalysis has raised that value to 0.78 (Kuo et al. 2007). We note that the value of σ_8 is still quite uncertain, and that recent measurements of cosmic shear (e.g., Semboloni et al. (2006); Hoekstra et al. (2006)) , the galaxy bispectrum (Scoccimarro, private communication), and the small-scale angular power spectrum of the CMB (e.g., Bond et al. (2005); Kuo et al. (2007)) all suggest a higher value than we have adopted. As a higher σ_8 would result in more detected clusters, the dark energy constraints would be correspondingly tighter; e.g., for $\sigma_8 = 0.9$, the DES-SPT cluster dark energy figure of merit increases by about 60%.

Finally, we note that, in deriving the constraints in Fig. 1, we have not imposed theoretical priors on the parameters in the SZE mass-observable relation. Improved theoretical modeling of clusters (see §7.) should enable us to remove some of the freedom currently encoded by these nuisance parameters, thus reducing the errors on derived cosmological parameters.

2.4 Ancillary Science

As the largest virialized systems in the Universe, clusters provide interesting environments for studying the interplay between gas, galaxies, and dark matter. Understanding the formation of clusters, including the effects of non-gravitational feedback on the cluster gas, is a topic of great general interest. Turning the question around, understanding the impact of cluster environment on the formation and evolution of galaxies will add significantly to our understanding of galaxy formation in general. In addition, the strong lensing cores of massive clusters (§6.) will provide windows of high magnification to the high-redshift Universe, enabling pathfinder studies for future extremely large telescopes.

3. Weak Lensing

The gravitational bending of light by massive structures in the Universe distorts the images of distant galaxies. Weak lensing measurements are sensitive to the evolution of the mass power spectrum and to the distance-redshift relation, which enables them to probe the nature of dark energy (e.g. Linder 2003; Song 2005). Near a massive galaxy cluster, the tangential stretching of background galaxy images is strong enough to reconstruct its mass distribution. Here we are concerned with the much weaker but ubiquitous signal due to gravitational lensing by the large-scale distribution of mass in the Universe, termed "cosmic shear". Since this signal was first detected (Bacon et al. 2000; Van Waerbeke et al. 2000; Wittman et al. 2000; Kaiser et al. 2000), larger areas of sky have been surveyed and analysed using more sophisticated techniques (e.g., Semboloni et al. (2006); Hoekstra et al. (2006); Jarvis et al. (2006)).

The primary statistical measure of the cosmic shear is the shear-shear correlation function or its Fourier transform, the shear power spectrum, measured in source-galaxy redshift bins. The weak lensing dark energy constraints given in §1. rely solely on the shear power spectrum (Hu 1999). Since the foreground lensing dark matter is associated to a large degree with foreground galaxies, one can also measure the angular cross-correlation between foreground galaxy positions and source galaxy shear (galaxy-shear correlations). The

shear, galaxy-shear, and galaxy angular power spectra can be expressed as projections of the corresponding three-dimensional power spectra (e.g., Hu & Jain 2004),

$$C_l^{x_a x_b} = \int dz \frac{H(z)}{D_A^2} W_a(z) W_b(z) P^{s_a s_b}(k = l/D_A; z)\,, \tag{3}$$

where ℓ denotes the angular multipole, $a, b \in \{1, 2\}$, x_1 and x_2 denote the two-dimensional angular galaxy (g) and shear (γ) fields, and s_1 and s_2 respectively denote the three-dimensional galaxy (g) and mass (m) density fluctuation fields at redshift z. The weight functions W_1 and W_2 encode information about the galaxy redshift distribution and about the lensing efficiency. The dark energy density and equation of state affect these angular power spectra through geometric factors, *i.e.*, the Hubble parameter, the angular diameter distance, and the weight factors, and through the growth of structure, *i.e.*, the redshift- and scale-dependence of the three-dimensional power spectra P^{gg}, P^{mm}, and P^{gm}. It is also possible to extract a purely geometric probe of dark energy from the redshift dependence of galaxy-shear correlations (Jain & Taylor 2003; Bernstein & Jain 2003; Zhang et al. 2005; Hu & Jain 2004). For a given choice of cosmological parameters, the shape of the mass power spectrum P^{mm} is well constrained on large scales by CMB anisotropy data; on scales below ~ 10 Mpc it must be computed using N-body simulations (§7.). The power spectra involving galaxies, P^{gg} and P^{gm}, require in addition a model for how luminous galaxies are distributed with respect to the dark matter, i.e., for the galaxy bias, which we model either with the halo occupation distribution (e.g., Yoo et al. 2006) or with some other phenomenological bias model with parameters that are marginalized over.

For the measurement of the shear power spectrum, the statistical uncertainty is (Kaiser 1992)

$$\Delta C_\ell^{\gamma\gamma} = \sqrt{\frac{2}{(2\ell+1)\, f_{\rm sky}}} \left(C_\ell^{\gamma\gamma} + \frac{\sigma^2(\gamma_i)}{n_{\rm eff}} \right) \tag{4}$$

where f_{sky} is the fraction of sky area covered by the survey (0.12 for DES), $\sigma^2(\gamma_i)$ is the variance in a single component of the (two-component) shear, and $n_{\rm eff}$ is the effective number density per steradian of galaxies with well-measured shapes. The first term in brackets, which dominates on large scales, comes from cosmic variance, and the second, shot-noise term results from both the variance in galaxy ellipticities ("shape noise") and from shape-measurement errors due to noise in the images. This expression assumes the shear field is Gaussian; for the forecasts in §1., we only use information at $\ell < 1000$, where this approximation should be reasonable. At even smaller angular scales (larger ℓ), the measurement uncertainties in the power spectrum can be smaller than the theoretical uncertainties due to baryonic effects that are unmodelled in N-body simulations that contain only dark matter (White 2004; Zhan & Knox 2004; Lin et al. 2006); we will address this issue through the simulation program described in §7..

In addition to shear-shear and galaxy-shear two-point functions, we can also measure the shear three-point function or bispectrum as well as various galaxy-shear three-point correlations. Three-point correlations are induced by nonlinear gravitational evolution, and their dependence on cosmological parameters differs from that of the power spectrum. Inclusion of three-point information therefore improves dark energy constraints and, more importantly, makes them more robust to systematic errors, which generally affect the bispectrum differently than the power spectrum (Takada & Jain 2004; Huterer et al 2005); we quantify this statement below in at the end of §3.2.

3.1 Weak Lensing in DES

The DES will survey an area 30 times larger than any on-going weak lensing survey and measure shapes for approximately 300 million galaxies. While this greatly reduces statistical uncertainties, we must ensure that systematic errors in shear measurement, photo-z determination, and cosmological theory do not come to dominate the dark energy error budget (see §3.2). Because DES will measure shapes for moderately bright

source galaxies, $i < 24$, we can use existing survey data to quantify many of the characteristics of these galaxies that are relevant for weak lensing.

We base all of our cosmological forecasts on the current delivered image quality of the Blanco telescope and Mosaic II imager. Based on recent and long-term CTIO weather records, 0.9" is the median point spread function (PSF) for the Mosaic II imager during the DES observing season, and we adopt this as the fiducial value for DES. The DEcam instrument and upgrades to the telescope are designed to improve the image quality performance, taking better advantage of the excellent site, which has estimated median seeing of 0.65". As described in the Science Requirements and Technical Specifications Document of the DECam and DES Data Management projects, the as-designed DECam system is estimated to deliver 0.8" PSF for these median seeing conditions.

The size of the PSF, along with the depth of exposures, determines the effective sky density $n_{\rm eff}$ of galaxies that are useful for cosmic shear measurement. The empirical shape noise for large, well-measured galaxy images in exposures of comparable depth to the DES is $\sigma(\gamma_i) = 0.16$ (Sheldon et al 2004, Jarvis et al 2003); we use this value to define $n_{\rm eff}$ in Eqn. 4. To estimate $n_{\rm eff}$ for the DES, we study images taken by the HST GOODS (Dickinson et al 2004), artificially degrading them to the typical PSF and noise values expected for DES. As a check on this estimate, we perform the same procedure on a 900 sec CFH12K I-band exposure taken with median PSF of 0.63", with depth similar to that of DES i-band. Adopting a median DES PSF of 0.9" (see above), we infer $n_{\rm eff} = 12$ arcmin^{-2} when using combined measurements from the r, i, and z bands; we use this number for forecasts of the DES weak lensing performance. Note that this *effective* source density is smaller by about a factor of two than the *total* density of galaxy sources above the DES 10σ photometric detection limit, because it includes down-weighting due to measurement error, blurring by the PSF, and other effects.

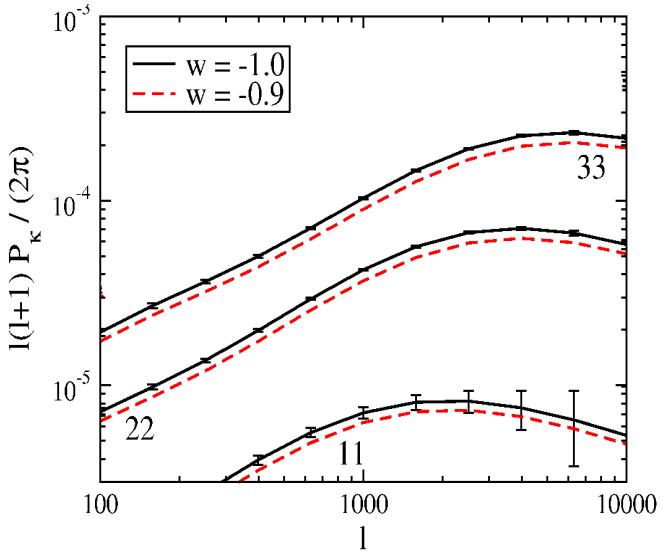

Figure 4: Angular power spectrum of cosmic shear for fiducial cosmology ($w = -1$, black) and for a dark energy model with $w = -0.9$ (red) in 3 photo-z bins of width $\Delta z = 0.5$, with binned statistical errors from Eqn.4. Not shown are the cross power spectra between different photo-z bins.

Fig. 4 shows the resulting predicted DES shear angular power spectrum in three photo-z bins of width 0.5 out to $z = 1.5$. The binned statistical errors from Eqn. 4 are also shown.

We find that $n_{\rm eff}$ increases by approximately 17% per 0.1" reduction in PSF around our fiducial PSF value, so the expected improvement in Blanco image quality upon installation of the DES optics and feed-

back systems should improve the signal to noise of the shear power spectrum measurement on small angular scales.

3.2 Weak Lensing Systematic Uncertainties

Systematic errors in weak lensing measurements can arise from a number of sources: incorrect shear measurements, uncertainties in the variance and bias of galaxy photometric redshift estimates, intrinsic correlations of galaxy shapes, and inaccuracies in predictions of nonlinear structure growth. We discuss our modeling of these effects below and summarize our findings on how much they potentially degrade dark energy parameter constraints in the summary at the end of this subsection.

PSF and Distortion Variation

The dominant galaxy shape measurement error in current lensing surveys is due to the *anisotropy* of the PSF caused by optical and CCD distortions, tracking errors, wind shake, atmospheric refraction, etc. In a given exposure, the PSF anisotropy as a function of angular position is measured using the stars in the field and interpolated to the positions of the galaxies. Because the density of stars is much lower than that of galaxies, interpolation errors can lead to coherent errors in the measured shapes of galaxies that are difficult to distinguish from the lensing shear. This leads to additive errors in the shear that must either be eliminated or marginalized over. The *static* part of the PSF pattern is easily controlled by combining different exposures to reach much higher stellar density across the field of view. The *time-varying* component of the PSF anisotropy can be more problematic, depending upon the angular and temporal scales of the variability.

Recently the error in interpolating the PSF shape has been substantially reduced by a Principal Component Analysis (PCA) technique that optimally uses information on the PSF from multiple exposures (Jarvis & Jain 2004), thereby enabling interpolation with much finer effective angular resolution. This is especially promising for the DES, since the technique has already been applied to data taken with the BTC and Mosaic II imagers on the Blanco telescope. Furthermore, Jain, Jarvis & Bernstein (2006) show that PSF patterns with variations on short time scales, such as due to instrumental effects varying with wind, gravity, and pointing, can be removed by cross correlating shears measured from different exposures (4-5 exposures are sufficient to apply this technique).

We have estimated how well the PSF patterns from the *existing* Blanco optics can be corrected using the PCA and cross-correlation technique for the survey parameters of the DES. The current level of raw PSF anisotropy in Mosaic II data is typically several %, and we estimate that we will be able to reduce it by over a factor of 100 for DES. This estimate is based on the analysis of Jain, Jarvis & Bernstein (2006), scaled conservatively to the number of exposures for DES (the correction improves with the number of exposures). The estimated residuals due to additive shear errors are well below the statistical errors expected for DES. Moreover, as noted below, ray tracing through the as-designed DECam corrector optics indicates that the level of raw PSF anisotropy will be around 1% percent over the DECam field of view, significantly below the current level in Mosaic II camera data.

Although PSF anisotropy systematics will be well under control for DES using the methods above, in order to physically understand and improve the optical quality and stability of the system we have carried out a detailed analysis of the optical distortions of the Blanco, using ray tracing simulations to model imaging data taken with the Mosaic II and BTC cameras. We can reproduce the dominant PSF distortion patterns empirically measured by Jarvis & Jain (2004) with (i) focusing errors coupled to astigmatism in the primary mirror, (ii) misalignments or tilts between the primary mirror and the optical axis defined by the camera and corrector, at a level consistent with measured misalignments, inducing coma, (iii) guiding errors, and (iv) trefoil distortions of the primary mirror associated with its support system.

DECam is being designed and the Blanco telescope upgraded to substantially reduce these systematic effects. The DECam optical corrector design does not include an atmospheric dispersion compensator (ADC), eliminating one source of coma. Its design achieves small and smoothly varying PSF distortions across the field of view, with an amplitude and angular dependence that meets our weak lensing requirements. After

convolution with atmospheric seeing of 0.6", the PSF ellipticity is everywhere below 1% in the *i* band at zenith and below 1.2% at 25 degrees from zenith. DECam will also be equipped with dedicated CCDs, absent from the Mosaic II, to provide continuous active control of the focus. In addition, wave front sensor chips in the focal plane will be used to continuously monitor collimation of the prime focus cage with the primary mirror, and the hexapod system will enable active recollimation. The telescope has been instrumented with position monitors to better understand the performance of the primary mirror support system and flexure of the telescope truss. Broken radial supports on the Blanco primary mirror have been identified as a primary source of misalignment; four newly designed supports were installed in October 2005, and the remaining 20 old supports will be replaced before DECam is installed.

Finally, our image simulations indicate that the DECam pixel scale of 0.27" should not be an issue for galaxy shape measurements, even if the DECam image quality is improved compared to that of Mosaic II. If the ratio of the pixel scale to PSF FWHM is below 0.36, then the object shape measurement is not degraded from optimal (Nakajima & Bernstein 2006); for multiple dithered exposures, this criterion can be further relaxed. For the very best conditions, say, atmospheric seeing of 0.3", the delivered PSF from telescope+instrument+site is expected to be $\gtrsim 0.56$"; while only a factor of two larger than the pixel scale, simulations indicate that shape measurements in these conditions, though noisy, would be unbiased (E. Sheldon, unpublished, 2005); again, in these conditions we will be sure to carry out multiple dithered exposures to effectively improve the image sampling.

Shear calibration

A second kind of shear measurement error arises due to miscalibration of the relation between measured galaxy shape and inferred shear and contributes a multiplicative error to the shear; it can arise, for example, from inaccurate correction for the circular blurring of galaxy images due to seeing. The finite size of the PSF and the distribution of intrinsic shapes of galaxies need to be accurately measured to calibrate the shear.

We have estimated the impact of shear calibration errors in the DES Fisher matrix forecasts by modeling in each redshift bin an independent shear calibration factor that is unknown and must be marginalized over when deriving dark-energy parameters. The prior knowledge of these calibration factors is given an *rms* uncertainty of 0.01 per bin, based on tests by Nakajima & Bernstein (2006) that demonstrate a shear recovery technique that reaches accuracy of 1% or better over a range of noise and resolution levels that span those to be expected in the DES data (see also Heymans et al 2006 and Massey et al 2007). Fig. 5 shows that this degrades the lensing constraints on w_0 and w_a (see §1.) by ~ 30 and 20 % respectively. Moreover, it is reassuring that calibration errors appear to be the least dangerous systematic for cosmological measurements (Huterer et al 2005). Unlike additive errors, with calibration errors there is less freedom in mimicking the redshift dependence of the shear signal. Hence even if the calibration errors are four times larger than expected (0.04 instead of 0.01), Figure 5 shows that the resulting constraints on w degrade by $40-70\%$.

Photometric redshifts

The impact of systematic photometric redshift errors on shear power spectrum measurements have been studied by Huterer et al. (2005) and by Ma, Hu, & Huterer (2006). The photo-z error distribution as a function of redshift can be characterized to lowest order by its scatter (width) and bias. Using a representative subsample of galaxies with measured spectroscopic redshifts, these quantities can be inferred empirically, with uncertainties depending on the size of the spectroscopic sample. Our shear power spectrum forecasts (§1.) assume an uncertainty in the photo-z scatter ($\Delta\sigma_z$) and bias ($\Delta z_{\rm bias}$) of 0.002 per redshift bin and marginalize over these quantities. As Fig. 11 shows, this leads to $\sim$ 10% degradation in the errors on w_0 and w_a compared to the ideal case. As discussed in §8., this level of uncertainty should be amply achieved with the spectroscopic samples that will be in hand prior to DES. Even if these uncertainties are substantially larger than expected, say 0.005, then the resulting degradation is less than 30% in w_0 and less than 50% in w_a.

Intrinsic alignments

Any tendency of galaxies to align with their neighbors—or to align with the local mass distribution—can

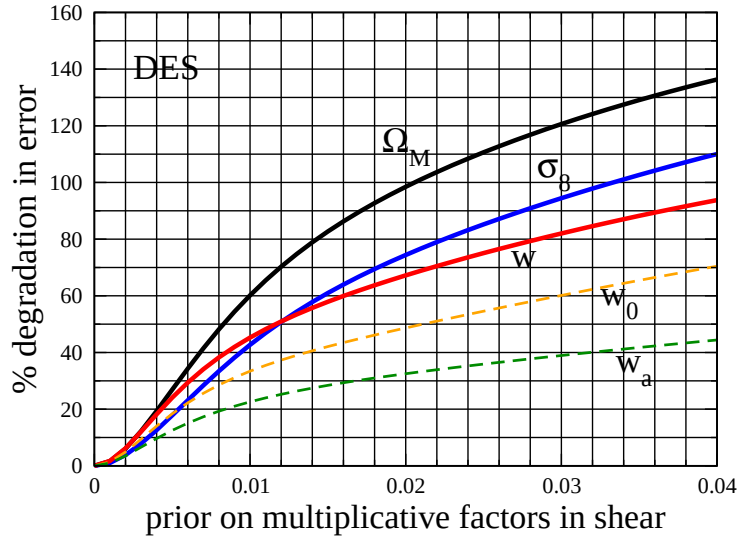

Figure 5: Degradation in forecast error on cosmological parameters from DES shear power spectrum, due to marginalizing over uncorrected multiplicative shear systematic errors in multiple redshift bins, from Huterer et al. (2005). Remaining cosmological parameters are marginalized over. The evolution of the dark energy equation of state, w_a, appears more robust than other parameters mainly because it is statistically less well constrained. The red curve marked w indicates a model with constant w (*i.e.*, with w_a set to zero); it is equivalent to the degradation in w_p.

be confused with alignments caused by foreground gravitational lensing, thus biasing dark energy determinations (Hirata & Seljak 2003). It is, however, possible to distinguish intrinsic alignments from true lensing once photometric redshift information is available for all source galaxies, because these effects have distinct redshift dependencies. There is some uncertainty about the size of the intrinsic alignment effect, and there are indications that excising a subsample of the red source galaxies will greatly reduce it (Mandelbaum et al 2006; Heymans et al 2006). For DES-quality data, we find that one can solve for lensing and intrinsic alignments simultaneously with only modest degradation of dark energy constraints if different lensing statistics (shear, shear-galaxy, and shear bispectrum) are combined.

Theory uncertainty

At sufficiently large angular scales, the matter distribution and therefore P^{mm} evolves according to linear perturbation theory, and the lensing signal is calculable to high accuracy for a given dark energy model. At smaller scales, N-body simulations of gravitational growth are required to predict the signal. The DES project will carry out numerical simulations of sufficient accuracy to exploit its weak lensing data (2% accuracy in the predicted matter power spectrum on the scales that contribute to $\ell \sim 1000$ lensing measurements), as described in §7.. At still smaller scales, baryonic effects become important and will also be simulated. We have tested our weak lensing forecasts by including redshift and scale-dependent uncertainties in the 3-dimensional mass power spectrum due to baryonic effects (White 2004, Zhan & Knox 2004, Jing et al. 2006) and marginalizing over them; we find that their effects on the forecast DES lensing dark energy constraints are negligible, even if they are significantly larger than expected. On the other hand, this suggests that those forecasts could be strengthened by including information from higher angular multipoles than we do in §1..

Systematic errors summary

We have estimated the effect of the four sources of systematic errors discussed above on weak lensing

Fisher matrix forecasts. Considering only the shear power spectrum, we find that shear calibration and uncertainties in photo-z errors and bias do not individually degrade the lensing dark energy figure of merit (FoM) given in Table 1 by more than 30-50% if the systematic errors are at the levels expected (see above); the effects of theory uncertainty remain negligible even if they are significantly worse than we have assumed (Huterer et al 2005; Huterer & White 2005; Huterer & Takada 2005). Intrinsic alignments between galaxy shape and the local mass distribution could substantially increase the cosmological errors from the shear power spectrum alone, in the pessimistic limit that we have no prior information on the amplitude of the effect.

When we add in information from galaxy-shear correlations and the shear bispectrum, however, then we see two effects: (i) for the same level of systematics, the dark energy constraints are significantly stronger than if we only consider the shear power spectrum; (ii) the dark energy constraints are much less sensitive to systematics than the power sepctrum alone. As an example of (i), if we include only photo-z systematics at the expected level, inclusion of galaxy-shear and the bispectrum increases the DES lensing FoM beyond that in Table 1 by about 70%. As an example of (ii), if we combine all four systematic errors at more pessimistic levels than we expect, the lensing FoM degrades by at most a factor of two compared to that in Table 1.

3.3 Weak Lensing Forecasts

The primary lensing statistic for cosmological constraints is the shear power spectrum measured in multiple redshift bins; Fisher matrix forecasts for dark energy parameters using this statistic alone are shown in Table 1 in §1.. These forecasts assume an analytic fit to the source galaxy redshift distribution with median $z_{med} = 0.68$, as expected from the photometric limits of the survey, an effective source galaxy density $n_{gal} = 12$ arcmin^{-2}, and 7 equally spaced photometric redshift bins between $z = 0$ and 2. We marginalize over the resulting 82 parameters used to characterize the photo-z error distributions (half of them describing redshift bias, half of them photo-z scatter); a prior of 0.002 is applied to each of the photo-z parameters, consistent with expectations from the spectroscopic training set (see §8.). For the shear power spectra, we use a maximum spherical harmonic number $\ell_{max} = 1000$ to avoid the uncertain effects of baryons on small scales. As noted above, this is a conservative choice, and we expect that there will in fact be useful information at higher ℓ.

4. Supernovae

Type Ia supernovae (SNe) provided the first direct evidence for cosmic acceleration (Riess et al. 1998; Perlmutter et al. 1999). In order to improve upon that evidence, a number of ambitious cosmological Supernova (SN) surveys, including the CFHT SNLS, ESSENCE, and SDSS-II SN, as well as several nearby searches and follow-up efforts, including the SNFactory, CSP, KAIT/LOSS, and CfA program are underway. By the end of the decade, these ground–based surveys will jointly deliver a Hubble diagram constructed from $\sim$ 1000 SN Ia light curves out to $z \sim 1$. Furthermore, searches using the Hubble Space Telescope (HST) are extending the SN Hubble diagram beyond $z \sim 1$ (Riess et al. 2007).

In combination with constraints from the CMB or from baryon acoustic oscillations in large-scale structure, supernovae currently provide some of the tightest constraints on dark energy parameters, and they remain the most mature observational technique for investigating dark energy (e.g., Astier et al. 2006). By the time of DES "first light," we anticipate that the limiting factor in cosmological constraints from SNe will not be statistical precision but rather systematic uncertainties associated with the observations (e.g., photometric calibration, survey completeness and Malmquist bias), with the analysis methods (e.g., K-corrections, light–curve fitting), and with the SNe themselves (e.g., dust extinction, progenitor bias, and evolution).

4.1 Supernovae in DES

The combination of the Blanco telescope aperture, wide field of view, and improved sensitivity of DECam is ideally suited to a new, high-redshift SN survey. The DES Supernova Survey is designed with the aims of improving both the statistical precision of SN cosmology and the control of systematic errors in

using SNe to measure distances, the dual goals recommended with high priority for Stage III projects by the Dark Energy Task Force.

While the wide-field DES strategy is fixed by the area, depth, and wavelength coverage requirements of the other three dark energy probes, there is more flexibility in designing the SN survey. The SN survey design is constrained by the limited observing time available, given the requirements of the wide-field survey and the 30% per year time allocation expected for the combined (wide-field plus SN) DES. Using simulations of the DES wide-field survey that employ 30-year historical weather records at CTIO, we have adopted a baseline time allocation of 750 hours over 5 years for the SN survey. Due to weather, the number of useable hours will be smaller, an effect included in the simulations below; on the other hand, we will be able to effectively 'queue-schedule' the SN observations within the DES observing runs, minimizing weather losses and ensuring relatively complete sampling of SN light curves. Roughly 40% of the SN time allocation includes non-photometric conditions that are not optimal for the wide-field survey; since the SN survey involves numerous repeat observations of the same fields, we can carry out relative photometry in useable non-photometric conditions. If the SN survey were to make full use of the useable non-photometric time, the total SN allocation could in principle be increased by about 30% from this baseline, based on median historical conditions, which could be used to improve SN data quality or quantity.

We are currently engaged in detailed Monte Carlo simulations of the DES SN survey, using the Blanco plus DECam parameters to simulate realistic photometric errors, generating multi-band SN Ia light curves from low-redshift templates, sampling from historical weather conditions at CTIO, fitting the resulting light curves to infer distances, and varying the area, depth, cadence, and filter choice of the survey within the time allocation constraint above. These trade studies will be used to help optimize the SN survey strategy, also taking into account the progress of the field expected over the next several years. Based on the design work to date, we present below a baseline SN survey which goes deep over a relatively narrow area of sky; for comparison, we also discuss an alternative strategy that is wider in area and shallower in depth.

4.1.1 Baseline SN Survey Strategy The baseline SN survey is optimized for high-redshift SNe, taking advantage of the enhanced red sensitivity of the fully depleted DECam CCDs to enable multi-band light curve measurements of substantially more SNe out to $z \sim 1$ with higher signal-to-noise than current ground-based surveys can achieve with reasonable exposure times. We assume 10, 30, & 50 min cumulative exposures per night in the r, i, and z passbands respectively, with a cadence of 5 visits per lunation. These exposure times correspond to 10σ point source limits of 24.8, 24.9, and 24.6 respectively in these three bands. For comparison, SNLS adopts a similar cadence in r and i and lower sampling rate in z, with typical exposure times of 25 minutes in r, 60 or 30 in i, and 60 minutes in z. However, given the larger telescope aperture of the Blanco vs. CFHT and the substantially higher CCD Q.E. in the red bands of DECam relative to Megacam (by factors of ~ 1.6 and ~ 4 in i and z), the effective DES SN depth is essentially identical to that of SNLS in i and substantially deeper in z. As a result, DES SN will have higher efficiency for detecting and accurately measuring light curves for SNe Ia out to redshifts $z \sim 1$. Its greater effective depth will reduce the effects of Malmquist bias, and the greater S/N in z band exploits its correspondence with rest-frame g at $z \sim 1$.

Given the time allocation noted above and including overheads for CCD read-out and telescope slewing, the baseline DES SN survey can cover 3 DES fields, i.e., 9 sq. deg., for 6 months of each year for 5 years; by comparison, SNLS covers 4 sq. deg. at an average of 5 months per field per year and the same 5-year survey duration. Thus, DES SN will cover about 260 sq.deg.-months, while SNLS will cover about 100 sq.deg.-months at somewhat shallower effective depth. As SNLS expects to reach $\sim$ 520 Ia light curves when completed, we expect $\sim$ 1400 Ia light curves from DES SN, in agreement with the predictions of our Monte Carlo simulation. The predicted redshift distribution for the subsample of $\sim$ 1100 Ia's with high-quality light curves is shown in Fig. 6 by the red histogram. For comparison, the approximate redshift distribution for the confirmed SNe Ia expected from the completed SNLS is shown as the black points.

Based on experience in fitting multi-band SN photometry in SDSS and SNLS to light curve templates

and comparing with follow-up spectroscopy, we expect the photometrically identified SN Ia sample to be $\gtrsim$ 95% pure Ia's even without spectroscopic follow-up. That is useful, because 'real time' spectroscopic follow-up of the full DES SN Ia sample is likely to be infeasible, given limited time resources on 6 to 10-m class telescopes. Nevertheless, to control the SN type-purity of the sample and to identify spectroscopically peculiar Ia's, we plan to pursue a campaign of spectroscopic follow-up on a subsample of $\sim$ 250 of the photometrically identified SNe, applying for public and private time on the VLT and GTC (through European DES collaborators), Gemini, Magellan, Keck, and the LBT. Assuming an hour's exposure per SN, this is a practical number to target for follow-up over 5 six-month seasons. In addition, we will aim to obtain host-galaxy spectra for the majority of the sample of $\sim$ 1000 photometric SNe Ia in the later years of the survey or after it is completed. This could be done efficiently using a combination of multi–object spectrographs such as FMOS, VIMOS, or AAOmega. In addition to providing accurate redshifts, this will enable us to probe SN systematics by searching for correlations between the metallicity, star–formation history, etc, of the hosts and SN properties. Using host galaxy spectroscopic redshifts will improve the SN light-curve fits and therefore the inferred SN distances; in addition, outliers between host spectroscopic redshift and SN photometric redshift provide an additional check on the Ia type-purity of the sample. Spectroscopic host redshifts for a large sample will also allow us to test the feasibility of doing SN cosmology without spectroscopic information, as envisioned for LSST; simulations indicate that, if Ia sample-purity can be controlled at the level above, then SN photo-z's should be sufficiently accurate for this purpose.

One option for achieving improved control of SN systematics is to focus resources on the $\sim$ 270 well-measured SNe Ia expected in elliptical hosts. Uncertainties in correcting for host galaxy dust extinction appear to be the dominant source of systematic error in inferring SN Ia distances in current surveys. Ellipticals are relatively dust-free environments, so that the uncertain extinction correction can essentially be eliminated. Also, since they are dominated by old stellar populations, the progenitors for elliptical Ia's should form a homogeneous class, compared to Ia's in star-forming galaxies which can come from both old and young stellar populations (see, e.g., Filippenko & Sargent 1989; Hamuy et al. 1996; Riess et al. 1999; Hamuy et al. 2000). To the degree that the progenitors are more homogeneous, one expects elliptically-hosted SNe to have smaller dispersion in peak luminosity; based on a relatively small sample, there is some evidence that this is the case (Sullivan et al. 2003). Finally, core collapse supernovae have not been found in ellipticals, so the efficiency for selecting Ia's in elliptical hosts should be very high.

There is some flexibility in positioning the SN fields on the sky. To minimize loss of efficiency due to survey duration 'edge effects' one could position the 3 SN fields to allow maximal exposure time at low air mass over the six-month SN season, Sept.-Feb., with minimal Galactic dust extinction. This strategy would bunch the 3 SN fields into a relatively narrow range of right ascension, RA $\sim 3-5$ hr. An alternative would be to split the six-month season into two halves, and to spread the resulting 6 fields over a broader range in RA. This would incur some fractional efficiency loss due to edge effects, but it would allow more efficient spectroscopic follow-up on large, non-queue scheduled telescopes. Moreover, we can boost the yield of SNe Ia in ellipticals by pointing the DES SN fields at previously detected, very rich galaxy clusters in the redshift range $z \sim 0.6-1$.

Finally, while the baseline SN survey uses riz filters, we will use simulations to explore the trade-offs of including the Y-band in the SN fields, since such a filter is already planned for DECam and will likely be used in the DES wide-field survey (see §8.4).

4.1.2 Wide SN Survey An alternative to the baseline deep SN survey would be to carry out a wide survey, as described in the DES white paper for the Dark Energy Task Force (DES collaboration 2005). With the same time allocation as above, the wide SN survey could cover, e.g., 70 deg^2 in r, i, and z with the same cadence and with exposure times of 200s in r, 400s in i, and 400s in z. This survey would have a SN redshift distribution similar to that of the ESSENCE survey, with median redshift $\sim$ 0.5, but it would obtain $\sim$ 2500 well-measured Ia light curves to $z < 0.8$, more than an order of magnitude larger than the expected final ESSENCE sample. The wide SN survey would discover a sufficient number of low-z

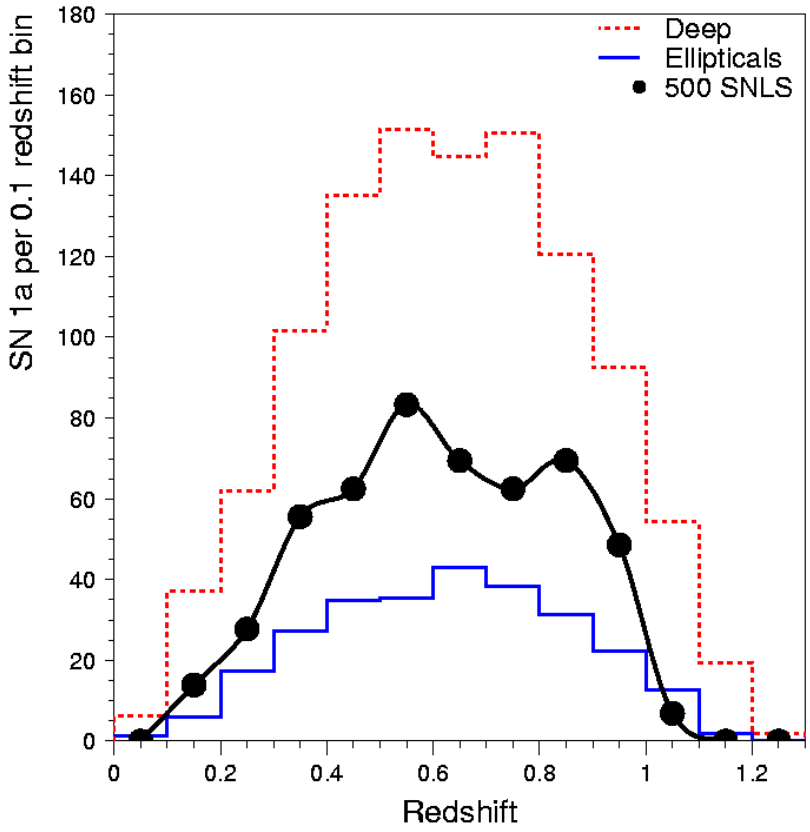

Figure 6: The distribution of expected redshifts for the 1100 SNe Ia in the baseline deep DES SN survey (red) and for the subsample of 270 Ia's in ellipticals (blue). For comparison, the expected distribution for the 520 Ia's from the anticipated complete 5 year SNLS is also shown (black).

SNe Ia (at $z < 0.15$) for both "re-training" the light-curve fitting templates and for anchoring the Hubble diagram and would therefore enable robust SN dark energy constraints using a *single*, uniformly calibrated dataset without the need for external calibrations. This strategy would eliminate the systematic uncertainty in photometric calibrations when combining different datasets as a function of redshift. This SN sample will also be large enough that it can be sliced into a large number of subsamples to study systematic effects. An additional $\sim$ 2000 SNe Ia with lower-quality light curves will be detected according to the Monte Carlo simulation; these will be primarily at higher than the median redshift.

4.2 Supernova Systematic Uncertainties

While increasing statistical precision compared to on-going SN surveys by a significant factor, the DES SN survey also aims directly at reducing the primary systematic errors associated with SNe. By focusing follow-up resources on ellipticals, we will substantially reduce the large current uncertainties due to dust extinction. Since ellipticals comprise a homogeneous, old stellar population out to at least $z \sim 1$, this SN sample will also be relatively free of evolutionary effects caused by the changing mix of progenitor populations with redshift. The survey strategy is focused on obtaining well-sampled, high-quality light curves in i-band and, more importantly, in z-band, out to redshifts $z \sim 1$; the latter is not feasible with currently deployed mosaic CCD detectors. At $z \sim 1$, observer-frame z-band corresponds to rest-frame g, while observed i and r correspond to rest-frame u and UV. Since nearby SN Ia light-curves and spectra are

still relatively poorly characterized in and show larger peak luminosity scatter in rest-frame *u* and bluer (Jha et al. 2006), the enhanced signal to noise in *z*-band for DES SN will be important for determining accurate SN distances at these highest redshifts available to ground-based photometry.

Another major source of systematic uncertainty is the ability to obtain accurate colors of SNe, as this directly translates into a luminosity correction factor. A new laser calibration system built by C. Stubbs, which has been prototyped on the Blanco, is being considered for long-term deployment. It should provide a filter-to-filter zero-point uncertainty of 0.01 mag, which translates into a peak magnitude uncertainty below 0.02 mag. Furthermore, if needed, the self-calibration technique proposed in Kim & Miquel (2006) can be used to reduce the sensitivity of the cosmological results to the color calibration uncertainty by a factor of a few. The price to pay is the loss of a cross-check on color evolution as a function of redshift.

An additional systematic noted above is photometric zero-point offset between low- and high-redshift SN samples measured with different instruments on different telescopes. This can be removed directly with the wide SN strategy. For the baseline deep survey, we will aim for a $\lesssim 0.01$ mag photometric zero-point offset between our sample and the low-z anchor sample, most notably, the SDSS-II SN Survey, by calibrating off the same standard stars (e.g., by placing one or more of our SN fields in SDSS stripe 82), and by using accurate measurements of the DES and SDSS filters and SN spectra to synthesize relative color terms. Our simulations show that marginalizing over an uncertainty at this level translates into a negligible increase of the overall uncertainty on w_0 and w_a. Even doubling this residual zero-point offset produces only a marginal increase in the dark energy uncertainties. K-correction uncertainties will be minimized by using a library of spectra tied to the same low-z photometric sample (e.g., SDSS-II), by exploiting the large samples of Ia spectra that a variety of groups have been accumulating in recent years (e.g., the CfA group), as well as improved multi-epoch spectrophotometric templates that the SNFactory is aiming to produce in the next few years. We will control Malmquist bias by acquiring high S/N measurements in at least two filters, ensuring that we sample the bulk of the instrinsic SN luminosity distribution out to $z \sim 1$.

For the fraction of SN events that will not be followed up spectroscopically, the SN type will be inferred from the photometric data alone and from host redshift information. By ensuring that we acquire high-quality light curves in 2 to 3 bands at all redshifts, we should be able to achieve high Ia sample purity. A small fraction (perhaps up to $\sim$ 5%, depending on light-curve quality and color cuts) of our photometric sample, however, may be contaminated by core-collapse SNe, primarily of type IIn and a very small number of luminous type Ibc's. We will use simulations and data from on-going surveys to select quality cuts to minimize sample contamination while maintaining high completeness. Light curve fits using post-survey host-galaxy redshifts will enable more robust expulsion of non-Ia contaminants.

4.3 Supernova Forecasts

For the SN dark energy forecast shown in §1., we use the parameters of the baseline deep survey, augmented with the local anchor sample of 44 nearby SNe used in the recent SNLS and ESSENCE analyses, and with an intermediate-redshift sample of 200 SNe centered at $z = 0.2$ from the SDSS. These numbers for the low-redshift samples are conservative, since they do not include on-going contributions from KAIT-LOSS, CSP, CfA, and SNFactory. For the DES SN sample, we use the baseline redshift distribution shown in Fig. 6. For the statistical errors in SN distances, we assume an intrinsic scatter of 0.12 mag in peak luminosity after correction for the brightness-decline relation (Phillips 1993); we add in quadrature a redshift-dependent scatter that reflects the increasing photometric errors with depth, which we model approximately by doubling the total scatter at $z > 0.8$.

In order to approximately account for systematic uncertainties, in the forecast we have assumed an irreducible error floor of 0.02 mag in each redshift bin of width 0.1 for SNe Ia detected in non-elliptical hosts, for which extinction corrections are the primary concern. That is, a 0.02 mag uncertainty is added in quadrature to each SN peak magnitude, fully correlated for all SNe in the same redshift bin, and uncorrelated otherwise (e.g., Frieman et al. (2003)). This systematics model motivates surveys with broader redshift

coverage, as opposed to just increasing the raw number of SNe, as the route to improved cosmological constraints.

4.4 Ancillary Science

Although cosmology with SNe Ia (and possibly SNe II-P) is the primary goal of the DES SN survey, there is other time-domain science that can be pursued with this data. Since the readout time for DECam is small, the SN exposures within a given night can be broken into a number of relatively short exposures, allowing us to search for fast transients that vary on timescales less than a day. Moreover, a carefully chosen exposure strategy will also allow us to distinguish SN candidates from moving objects (asteroids and Kuiper belt objects), which are typically the main source of contamination (along with AGN) in SN searches.

This rolling time-domain survey will also discover and measure light curves for many other variable objects including active galactic nuclei and QSOs, core-collapse SNe, afterglows of cosmic gamma-ray bursts, and possibly rare events like tidal disruption flares from supermassive black holes. We will plan to disseminate these detections to the astronomical community on the same timescale that the data are processed, to enable rapid follow-up observations.

5. Baryon Acoustic Oscillations

Oscillations of the coupled photon-baryon fluid in the early Universe imprint a "standard ruler" scale on the pattern of matter clustering. This baryon acoustic oscillation (BAO) scale, set by the sound horizon scale at the epoch of recombination, can be calculated from straightforward physics and calibrated by its projection in the CMB. In the galaxy correlation function, $\xi_{gg}(r)$, the BAO signature is a sharp local peak at $r = 150$ Mpc. In the galaxy power spectrum, the Fourier transform of this peak appears as a series of oscillations, analogous to but more subtle than the acoustic oscillations in the CMB power spectrum. Measuring the BAO scale from galaxy clustering in the transverse and line-of-sight directions yields estimates of the angular diameter distance $D_A(z)$ and Hubble parameter $H(z)$, respectively (Seo & Eisenstein 2003; Blake & Glazebrook 2003). While determining these quantities with high precision requires enormous survey volumes, current theory suggests that the systematic uncertainties associated with BAO distance scale measurements are smaller than those of other observational probes of dark energy.

BAO features have been detected at high statistical significance in the correlation function (Eisenstein et al. 2005) and power spectrum (Percival et al. 2006ab; Tegmark et al. 2006) of Luminous Red Galaxies (LRGs) from the SDSS, and in the power spectrum of galaxies in the 2dFGRS (Cole et al. 2005). The cosmological constraints from the SDSS are substantially sharpened by the BAO measurement (Tegmark et al. 2006), which effectively determines the comoving distance to redshift $z = 0.35$. Most directly relevant to the prospects for DES, recent studies of the angular clustering of photometrically selected LRGs from the SDSS provide precise measurements of the galaxy power spectrum and clear detection of BAO features in photometric redshift bins out to $z \sim 0.6$ (Blake et al. 2006; Padmanabhan et al. 2006).

In addition to the relatively sharp BAO features, the matter power spectrum has a gradual break that depends on the horizon scale at matter–radiation equality. The broad-band shape of the galaxy power spectrum thus provides an additional standard ruler.

5.1 BAO in DES

The sample of ~ 300 million galaxies with accurate photo-z's, $\sigma(z) \sim 0.08$, to $z \sim 1.4$ (see §8.) provided by DES is extremely well suited for measurement of BAO to study dark energy. The survey volume is 20 times that of SDSS photometric LRGs (Blake et al. 2006; Padmanabhan et al. 2006), enabling much higher precision measurements over a much wider redshift range. Statistical errors in BAO measurements arise from the finite survey volume (sample variance) and shot noise of the galaxy tracers. Out to $z = 1.4$, sample variance dominates the errors for DES BAO on the scales of interest; using VISTA-IR data to push DES photo-z measurements to higher redshift (§8.), shot noise would become comparable to sample variance at $z = 1.55$. If one chooses to analyze clustering of LRGs only, shot noise would become comparable

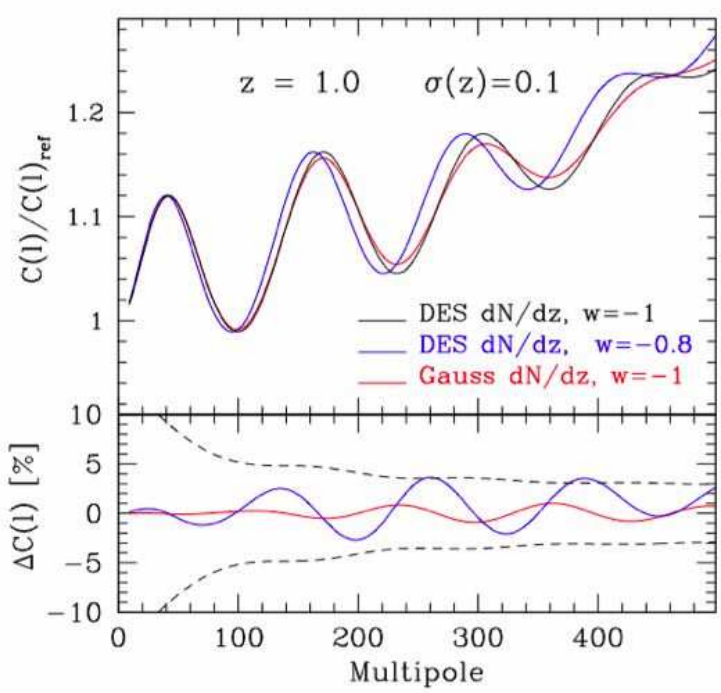

Figure 7: Top panel shows the angular baryonic acoustic oscillations for a redshift slice of thickness $\Delta z = 0.1$ at $z = 1$, calculated by dividing the non-linear angular power spectrum C_l for $w = -1$ (black) and $w = -0.8$ (blue) by a linear theory model with no BAO. For this plot, we used halofit (Smith et al. 2003) to model the non-linear clustering. The red curve shows the effect on the BAO signal in the $w = -1$ case when using photo-z's with standard deviation of $\sigma_z = 0.05$ per galaxy. Bottom panel shows statistical errors for DES in multipole bins of $\Delta l = 30$ (dashed lines), compared to the percentage differences of the blue and red curves of the top panel from the fiducial (black) model.

to sample variance at $z = 1.4$, so this approach could extend the redshift range, but with steadily decreasing precision.

The simplest approach to BAO in a multi-band imaging survey is to divide the sample into photo-z bins and measure the angular power spectrum in each. It is possible that a "global" method that does not divide the sample into photo-z bins would be better; however, since the typical photo-z error corresponds to a distance not much smaller than the BAO scale, we expect most of the information in DES to come from transverse clustering, with little additional information from the galaxy distribution along the line of sight. The angular power spectrum within a redshift shell can be written as

$$C^i_{\rm gal}(l) = \int_0^\infty k^2 dk \, \frac{2}{\pi} \, f_i^2(l,k) P_{\rm gal}(k), \tag{5}$$

where $f_i(l,k)$ is the Bessel transform of the radial selection function for redshift shell i (Tegmark et al. 2002, Dodelson et al. 2002).

As an example, the predicted angular power spectrum in a redshift slice of width $\Delta z = 0.1$ centered at $z = 1$ is shown for two dark energy models in the upper panel of Fig. 7; to more clearly display the BAO signature, a linear perturbation theory power spectrum with $w = -1$ and no baryons has been divided out. A change in the dark energy equation of state induces a shift in the positions of the BAO peaks and troughs. The bottom panel shows the binned statistical errors (dashed curves) compared to the percentage

difference between the constant $w = -1$ and $w = -0.8$ models as a function of angular multipole. As the plot suggests, for this single redshift slice, the statistical error on constant w is $\delta w = 0.2$; combining data from multiple redshift slices leads to the constraints shown in §1..

In addition to sample variance and shot noise, the statistical significance of BAO detection depends on the precision of photo-z estimates. Fig. 7 (red curve) illustrates the effect on the angular power spectrum of including a photo-z error of $\sigma_z = 0.05$ per galaxy, slightly better than we expect to achieve with DES (§8.). The amplitude and therefore the statistical significance of the BAO signal is reduced as photo-z errors increase, but the angular position of the feature is essentially unchanged. This reduction of BAO signal-to-noise is included, using realistic photo-z precision for DES, in the forecasts of §1.. The bottom panel of Fig. 7 indicates that it results in a modest increase in the cosmological errors from BAO.

As with weak lensing, DES angular clustering measurements can be extended to higher orders, i.e., to the bispectrum and beyond. The bispectrum carries additional information beyond that in two-point statistics that can be used to constrain galaxy bias, to control systematic errors (§5.2), and to increase the cosmological precision of angular clustering constraints (Dolney et al. 2006; Sefusatti et al. 2006).

While our cosmological parameter forecasts use only the *shape* of the galaxy power spectrum, we will also explore using the full *amplitude* information contained in the power spectrum. Unlike the power spectrum shape, which provides a purely geometric probe of dark energy–similar to supernovae–the redshift dependence of the amplitude depends on and thereby constrains the growth rate of large-scale structure, yielding complementary information on the nature of dark energy. The statistical errors on the power spectrum amplitude are smaller than the corresponding errors on the shape, but the systematic uncertainties are quite different. This approach requires more detailed modeling of galaxy bias and more accurate control over the galaxy selection function than the power spectrum shape measurement. On large scales, galaxy bias can be self-calibrated to a few percent accuracy using the reduced bispectrum (see, e.g, Sefusatti & Scoccimarro 2005). Marginalizing over the shape information, the amplitude of large–scale clustering constrains the linear growth function in a way that is independent of the modeling of the primordial spectrum or the matter transfer function. Given the wide range of redshifts covered by the DES, there is great potential in this approach.

5.2 BAO Systematic uncertainties

The primary systematic errors in applying the BAO technique naturally fall into two classes, (i) limitations in cosmological and astrophysical theory, and (ii) biases in the measurements themselves. We discuss these in turn.

The main theoretical uncertainties in the interpretation of BAO measurements are the effects of non-linear gravitational evolution and of scale-dependent bias between galaxies and dark matter. Non-linear evolution erases the acoustic oscillations on small scales, while both non-linear mode coupling and scale-dependent bias can shift the positions of the BAO features. Several numerical studies to date suggest that the resulting shifts of the BAO peak in the correlation function are at most $1-2\%$ (Seo & Eisenstein 2005; Springel et al. 2005; Guzik, Bernstein, & Smith 2007), although Smith et al. (2006) find potentially larger shifts, depending on halo mass. In any event, the simulation program described in §7., as well as other simulations that will become available over the next few years, will enable us to calculate the corrections due to non-linearity and scale-dependent bias to sufficient accuracy that the remaining systematic uncertainty will be small compared to the DES statistical errors on large scales; indeed, these simulations will determine how large the scale must be for the above statement to be robust. These studies will also investigate the dependence of the observable oscillation scale on the cosmological model itself, since the non-linear and galaxy bias effects could vary with the dark energy parameters that one is trying to extract (see §7. for more details). In addition, since the bispectrum responds to non-linearity and bias differently from the power spectrum, measurement of the angular bispectrum shape in DES will provide a cross-check on these effects.

Scale-dependent bias on large scales is potentially more of a concern for interpreting the broad-band

power spectrum shape than for the BAO signal. Again, the simulations described in §7., as well as measurement of the bispectrum, will help constrain this scale-dependence and determine the efficacy and robustness of including the broad-band shape in constraining dark energy.

Beyond these two effects, redshift-space distortions have a second order effect on the angular clustering measurements, as they move galaxies between redshift slices. (By contrast, for spectroscopic BAO surveys, redshift distortions have a first order impact on radial clustering.) The change in power spectrum amplitude due to this effect will vary smoothly with scale and consequently will not significantly affect BAO scale measurements, but it will have to be modelled when fitting the broad-band power spectrum shape. This issue will be addressed by the planned simulations as well.

In addition to these theoretical uncertainties, there are sources of systematic error associated with the measurements themselves: uncertainties in photometric redshift errors and photometric redshift biases, and photometric zero-point drifts over the survey.

The dependence of the BAO signal amplitude on the fiducial value of the photo-z error σ_z was noted above in Fig. 7 (red curve). In addition, BAO are in principle sensitive to the *uncertainty* in the variance, $\Delta\sigma_z$, and in the bias, Δz_{bias}, of the photo-z estimates in redshift bins. Fig. 11 shows the degradation in BAO constraints on w as a function of these quantities, which are treated as nuisance parameters that are marginalized in deriving cosmological parameter constraints. To ensure that the dark energy parameter constraints are degraded (i.e., the errors increased) by no more than 10%, these uncertainties in σ_z and z_{bias} per redshift bin of 0.1 must be kept below ~ 0.01 (for w_0) and ~ 0.005 (for w_a). As noted in §8., these performance levels should be comfortably exceeded in DES; based on the simulated photo-z errors and the size of the spectroscopic training sets that will be in hand, we have set a realistic requirement of 0.002 on these uncertainties. The BAO constraints are therefore expected to be quite insensitive to *uncertainties* in photo-z parameters.

Photometric zero-point drift affects the number density of galaxies in each redshift bin that lie above the detection threshold. We estimate that a $\delta m_{zp} \sim 0.01$ shift results in a fractional change in the number density $\delta n/n$ of detected galaxies that scales roughly linearly with redshift and reaches 0.7% at $z = 1$. To assess the impact this will have on the BAO measurement, one must model the angular power spectrum of the photometric zero-point drift. Assuming there are no preferred scales for the zero-point drift, a drift at the level of the DES science requirement, $\delta m_{zp} = 0.01$ over the scale of the survey area, would introduce an irreducible, fractional noise contribution in the angular power spectrum $\delta C_l/C_l \sim (\delta n/n)^2 = 1.4\%$. The DES survey strategy, with its multiply overlapping tiles, is designed to minimize photometric drifts and to make them negligible on the scale of the DECam field of view; any such residual drifts should appear only at much larger angular scales, $\ell \ll 100$, so the impact on the BAO constraint should be negligible. The extra power on large scales could potentially impact the broad-band power measurement and the inference of the horizon scale at matter-radiation equality with greater significance (a similar effect could arise from large-scale systematic errors in the correction for Milky Way dust extinction); again, the survey strategy is designed to keep such effects at very low ℓ, so they should be small compared to the statistical errors from sample variance.

In addition to direct control from the tiling strategy, we will have a number of internal cross-checks on such drifts, including the redshift evolution of the BAO and matter-radiation scales, cross-correlations between different photo-z bins, consistency with the angular bispectrum, and comparison of the power spectrum shape and features for different galaxy-type subsamples. Since the statistical errors are not dominated by shot noise, comparison of results from different subsamples offers a way to check for consistency without compromising statistical precision.

5.3 BAO Forecasts

DES power spectrum shape measurements (BAO and broad-band shape) were forecast using the same galaxy redshift distribution, photometric redshift binning, and photo-z error model as used above for the

weak lensing forecasts (§3.3). We use one galaxy bias parameter for each redshift bin and marginalize over these seven parameters as well. We use the halo model to calculate the non-linear galaxy power spectrum, and we conservatively use only information up to angular multipoles $\ell < 300$, where the clustering is close to the linear regime and the halo model of bias is most robust. We do not use bispectrum information in our forecasts; their inclusion could either be used to strengthen the statistical constraints or provide a cushion against systematic errors.

As noted above, the broad-band power spectrum shape is more sensitive than BAO to subtle scale-dependent galaxy bias on scales $> 100\,h^{-1}$ Mpc. While §5.2 describes a multi-pronged strategy for controlling this effect, in a worst-case scenario one could carry out the analysis using only the BAO and excluding information from the overall shape; in this case, the constant w constraints weaken by approximately a factor of two. On the other hand, we expect that, with improved theoretical modelling (§7.), we are likely to be able to robustly extend the BAO analysis to smaller angular scales than we have assumed; extension to $\ell = 700$ would strengthen the BAO constraints by a similar factor.

Also note that the BAO forecasts have not included the improved photo-z performance at $z > 1$ that will come from combining DES with VISTA-IR data, and they have not included constraints that would come from analysis of the more strongly clustered LRGs.

5.4 Ancillary science

In addition to setting constraints on dark energy, precise measurements of the galaxy power spectrum also constrain the primordial power spectrum, the physics of inflation, and the energy densities of neutrinos, baryons, and dark matter. Of these, perhaps the most interesting is the possibility of setting a constraint on the sum of the neutrino masses using the shape of the power spectrum, having constrained the background cosmological model with the BAO.

DES will provide an enormous, deep galaxy sample with multi-band data and photo-z's. We will use this sample to trace the evolution of the relation between galaxies and dark matter using halo occupation modeling for both two-point statistics and measures of higher order correlations. The high galaxy density means that this modeling can be constrained as a function of galaxy luminosity and color. Higher order correlations can also be used to constrain the initial conditions and the gravitational clustering paradigm (e.g., Bernardeau et al 2002).

6. Other Dark Energy Probes

The Dark Energy Task Force Report stressed the importance of employing multiple dark energy probes to achieve robust cosmological constraints and focused on the four primary techniques we have described above. Here we note that DES will enable other dark energy methods beyond these four, and we highlight two of them. These additional probes are not currently expected to provide statistical precision on dark energy at the level of the four primary techniques, but they do help provide qualitative and, being subject to different systematic errors, robust evidence for dark energy. Moreover, it is possible that theoretical or near-term observational developments will enable one of these techniques to emerge from DES as a more powerful quantitative rival of the four methods in probing dark energy. A well-designed survey such as DES will be positioned to take advantage of such potential developments.

6.1 Integrated Sachs-Wolfe: Cross-correlating DES galaxies with CMB

The decay of the gravitational potential when the Universe becomes dark-energy dominated leaves a signature in the CMB anisotropy in the form of the integrated Sachs-Wolfe (ISW) effect. This signature can be extracted by cross-correlating the CMB temperature with the galaxies in DES (Crittenden et al. 1996). Cross-correlating with WMAP, a non-zero ISW signal has been observed in the Luminous Red Galaxy sample and photometrically detected quasars in SDSS (Scranton et al. (2003); Cabre et al. (2006); Fosalba et al. (2003); Giannantonio et al. (2006); for a review, see Gaztanaga et al. (2006)). DES, which goes deeper over a similar area of sky that has been analyzed in SDSS, will certainly see this effect even

more prominently (Cabre et al. 2007). Recent work (LoVerde et al. 2007) suggests that the effect will be enhanced by gravitational magnification. Extracting robust constraints on the properties of dark energy will require an understanding of large-scale bias, which we will pursue through a range of simulations (§7.). The cosmological constraints that result are likely to be only slightly tighter than those from CMB experiments alone (Pogosian et al. 2005), but the success of the cross-correlation program could help inform the Stage IV dark energy experiments to follow.

6.2 Strong Gravitational Lensing

The frequency and nature of strong gravitational lensing events depend upon the dark energy. Expectations are (Kuhlen et al. 2004) that DES will discover of order 1000 strongly lensed QSOs and an even larger number of strongly lensed galaxies. The large sample of multiply imaged objects offers an important arena in which to apply various tests of dark energy (e.g., Chae (2003); Lewis & Ibata (2002); Kuhlen et al. (2004)); strong lensing can provide constraints in the w_0-w_a plane that are complementary to the techniques above (Linder 2004). Strongly lensed arcs in clusters are being found in increasing numbers using automated search techniques (e.g., Hennawi et al. (2006)); clusters exhibiting multiple arcs at different redshifts offer the possibility of a new geometric probe of dark energy (Link & Pierce 1998; Golse et al. 2002).

7. Large-Scale Structure Simulations

Testing the nature of dark energy through large-scale structure signatures requires the ability to accurately predict sky survey expectations for a given world model. The large-scale structure (LSS) team within DES will employ a variety of simulation methods to address cluster (CL), weak lensing (WL) and baryon acoustic oscillation (BAO) survey signals.

Because the power spectrum of matter fluctuations at recombination is calculated to high accuracy from linear theory (Seljak *et al.* 2003), the problem of realizing the emergence of non-linear structure in a particular world model is well posed as an initial value problem. At a basic level, simulation support for DES science involves realizing multiple simulations of Hubble Length dimension within which the principal clustered matter components — dark matter and multiple phases of baryons, including stars and cold gas in galaxies, warm/hot gas surrounding galaxies and in groups/clusters — are represented by multiple, coupled fluids. Two fundamental barriers stand in the way of a complete solution to this problem: i) the wide dynamic range of non-linear structures and ii) the complexity of astrophysical processes that control the baryonic phases. While the first issue is not strongly limiting for DES (which probes galactic and larger scales at late cosmic times), the second is currently a limiting issue for galaxy and cluster studies,

We will employ complementary approaches in three key areas of the full large-scale structure formation problem. A halo model description of the density field, which posits that all matter is contained in a spectrum of bound halos characterized primarily by their mass M, ties these approaches together (Berlind & Weinberg 2002; Cooray & Sheth 2002).

7.1 Precision measurements of dark matter clustering

We will use large simulations of collisionless clustering of dark matter to address the non-linear evolution of the matter power spectrum $P(k)$ and to improve the characterization of the space density, clustering bias, and internal structure of the dark matter halo population as a function of mass.

Currently, matter power spectra are known into the mildly nonlinear regime ($k \sim 1/\mathrm{Mpc}$) to 1-2% (Heitmann *et al.* 2005). At higher wavenumbers, the uncertainty grows to 5-10 % at the resolution limits of the codes. We have embarked on production of large-volume N-body simulations, with the aim of lowering uncertainties in $P(k)$ to the 2% level at $k \sim 5/\mathrm{Mpc}$. With a 10^6 processor-hour allocation on a $10,240$-processor IBM supercomputer (Marenostrum) at Barcelona Supercomputer Center (BSC), Gaztanaga's group have produced a nested set of 10^9-particle simulations in volumes of length 750, 1500 and $3000h^{-1}$ Mpc in a concordance ΛCDM cosmology. After a recent Marenostrum upgrade, we have begun

10^{10} particle simulations of the same-sized volumes. We plan to run a similar set of models in cosmologies with $w \neq -1$ and $w' \neq 0$, using BSC and NCSA resources.

These runs will produce large ($N > 10^4$) samples of halos that will be used to test the universality of similarity solutions for the halo space density (Jenkins *et al.* 2001, Warren *et al.* 2006, Reed *et al.* 2006) and spatial clustering (Seljak & Warren 2004) at the few percent level across the mass range $10^{13} - 10^{15}\, h^{-1}\, M_\odot$. The overlapping dynamic range of the nested simulations will allow us to address systematic uncertainties in galaxy assignment schemes discussed below. These models will also be used to produce sky surveys extending to redshifts $z \simeq 1.5$ with at least an order of magnitude better mass resolution than the Hubble Volume simulation (Evrard *et al.* 2002).

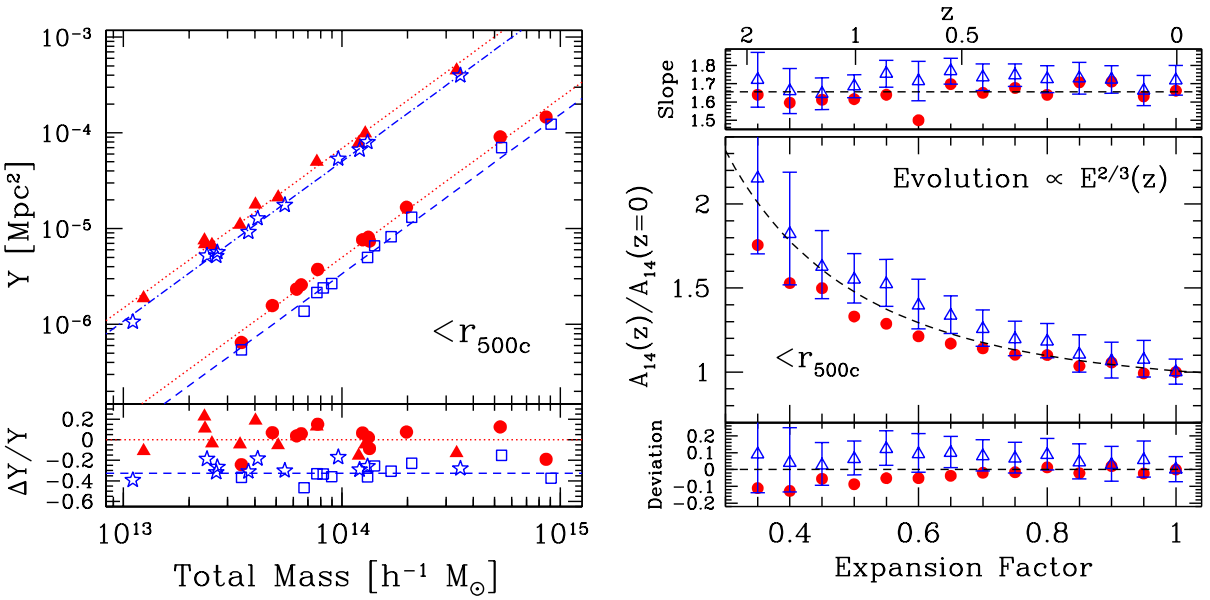

Figure 8: *Left:* Correlation between integrated Sunyaev-Zeldovich (SZ) flux decrement Y and total cluster mass M in ART simulations with (blue points) and without (red points) radiative cooling at two different redshifts. Both quantities are measured within the radius that encloses a mean interior mass density of 500 times the critical density, a scale that captures most of the expected cluster SZ signal and that is accessible to SPT. Points at $z = 1$ (upper) and $z = 0$ (lower) are displaced by a factor of 10 for clarity. The relation remains tight in simulations that include cooling and galaxy formation. *Right:* Evolution of the slope and normalization of the power-law mean $Y - M$ relation. Models with or without star formation closely follow self-similar expectations (dashed line). Adopted from Nagai (2006).

7.2 Astrophysical modeling of baryon components

We are pursuing an aggressive program of N-body+gas dynamic simulations, using multiple codes and modeling approaches, to probe the detailed form of intrinsic halo scaling relations. Specifically, we plan to: i) measure the covariance among optical and hot gas properties as a function of halo mass and redshift, ii) place bounds on extreme behavior and investigate the nature of outliers in scaling relations, and iii) determine the forms of redshift evolution that arise for specific astrophysical models. By exploring a range of such models, we will identify parameter degeneracies and search for signatures that would minimize astrophysical uncertainties on the DE figure of merit.

One line of investigation is employing gas dynamic resimulations of the Millennium Simulation (Springel *et al.* 2005) to generate samples of thousands of high-mass halos. The full MS volume has been evolved twice with gas under GADGET, with different treatments for gas evolution, and a third is under production.

In addition, we will evolve a sub-sample of MS clusters with the AMR code FLASH (Fryxell et al. 2000), which follows the dynamics of dark matter, gas, and stars and includes radiative cooling and feedback from supernovae. The system state of each simulation is stored at 160 epochs, allowing sky survey production and the detailed investigation of dynamical evolution behavior of outliers (Randall, Sarazin, & Ricker 2002). The large ensemble of MS halos will be used to investigate the form of the covariance in mass-observable relations and its sensitivity to the assumed physical model. Knowledge of covariance will lead to improvements in the DE figure of merit from clusters through improved modeling of the survey selection function.

This approach will be complemented with high-resolution, multi-component modeling using the parallel ART N-body+gas dynamics code (Kravtsov 1999, Kravtsov *et al.* 2002). Fig. 8 shows results from a pilot sample of 16 high-mass clusters simulated at high spatial resolution ($\sim 2h^{-1}$ kpc) with a non-radiative treatment and with gas dissipation and star formation feedback (Nagai 2006; Nagai *et al.* 2006, Kravtsov *et al.* 2006). The models exhibit a tight relation between mass M and the integrated electron pressure Y, the signal probed by SPT observations of the thermal SZ decrement. Because galaxy formation in cluster environments is inefficient and peaks at high redshift, $z \geq 2$, the evolution in the $Y - M$ relation at $z < 1.5$ departs only weakly from the self-similar case expectation of purely gravitational clustering. Early galaxy formation also means that a well-defined ridgeline of red galaxies emerges in massive halos at these epochs (DeLucia *et al.* 2006). We are extending this analysis to a factor ten larger ensemble of simulations designed as a complete, mass-selected sample with $M > 2 \times 10^{14} h^{-1}$ M$_\odot$ in a ΛCDM cosmology.

7.3 Mock Sky Surveys of Galaxies and Clusters of Galaxies

For the large-volume N-Body and MS gas simulations, we will map the numerical solutions along the past light-cone of synthetic observers to produce sky survey realizations of dark matter, hot gas signatures and galaxies. These surveys will be used within the collaboration to calibrate projection effects and astrophysical systematics, to tune cluster finding algorithms and weak lensing analysis, and to provide a testbed for cluster self-calibration exercises.

We will use multiple complementary methods to include galaxies. One is a semi-empirical method, ADDGALS (Adding Density Determined Galaxies to Lightcone Simulations, Wechsler et al 2007) designed to get maximum benefit from large, low resolution simulations. This approach populates the dark matter density field with galaxies brighter than the DES magnitude limit in a manner constrained to match the observed color, magnitude and scale dependence of the two-point galaxy correlation function. The technique has been used to populate sky survey octants of the Hubble Volume simulation with galaxies down to $0.4L_*$ and extending to $z \sim 1.4$. We will apply the same method to the lightcone simulations from Barcelona, using the range of sizes to explore sensitivity to mass resolution and to create surveys that push to dimmer galactic magnitudes.

A second approach will populate halos using an occupation function $P(N|M)$ that specifies the probability that a halo of mass M contains N galaxies in a specified range of luminosity and color (Berlind and Weinberg 2002). The occupation function can be predicted by theory or derived empirically through clustering data. A third approach uses halo substructure in high resolution simulations as a basis for galaxy assignment. Conroy *et al.* (2006) show that a model mapping luminosity to the sub-halo circular velocity at its time of accretion provides an accurate match to the luminosity and scale-dependent two-point clustering of galaxies from $z \sim 5$ to the present. With available simulations, this method can model galaxies in the range $-18 < M_r < -22$ within a $(400h^{-1}\mathrm{Mpc})^3$ volume. In addition to these, the direct ART simulations and semi-analytic models applied to the MS simulation offer first-principle channels to galaxy formation predictions.

As the DES data come in, we will refine our models based on the measured relations between luminosity, color and spatial density. Pursuing the above combination of first-principles and empirical approaches will allow us to make combined assessments for systematic uncertainties in weak lensing, BAO and cluster signatures.

Members of the LSS simulation group bring extensive, varied, and mutually complementary expertise in core areas needed to address the science areas above. This expertise includes designing simulation algorithms and executing large N-body+ gas dynamic simulations, statistical methods and analysis, and extensive approaches to phenomenological application, particularly models of galaxy populations and construction of mock galaxy and cluster catalogs.

8. Photometric Redshifts

In order to achieve its scientific goals, the Dark Energy Survey will need to obtain accurate galaxy photometric redshifts (photo-z's). Detailed understanding of the photo-z error distributions, as functions of galaxy magnitude, redshift, and type, will be important for obtaining accurate cosmological parameter constraints. There are two basic approaches to measuring galaxy photometric redshifts. The first relies on fitting model galaxy spectral energy distributions (SEDs) to the imaging data, where the models span a range of expected galaxy redshifts and spectral types (e.g., Sawicki et al. 1997). The second approach depends on using an existing spectroscopic redshift sample as a training set to derive an empirical photo-z fitting relation (e.g., Connolly et al. 1995; Collister & Lahav 2004). There are advantages and disadvantages to each approach, as well as a good number of variants and hybrids of these basic techniques (e.g., Csabai et al. 2003). However, photo-z methods ultimately rely on measuring the signal in the imaging data arising from prominent "break" features in galaxy spectra, most often the 4000Å break or the 912Å Lyman break. The key is to have photometric bands which cover such break features throughout the redshift range of interest, in order to readily detect the primary redshift signal.

8.1 Spectroscopic Training Sets

Training sets of $5 \times 10^4 - 10^5$ spectroscopic redshifts will be required in order for systematic photo-z uncertainties to not significantly degrade cosmological parameter constraints (Ma, Hu, & Huterer 2006), and we will rely on a number of ongoing or completed redshift surveys to provide the large samples needed for accurate DES photo-z calibrations. At bright magnitudes, the DES will rely on the Sloan Digital Sky Survey (SDSS) and the 2dF Galaxy Redshift Survey (2dFGRS). The DES area intentionally covers SDSS Stripe 82, which not only includes standard SDSS main galaxy and luminous red galaxy (LRG) spectroscopic redshifts, but also various deeper special SDSS samples down to $r \sim 20$. In total, some 70,000 SDSS spectroscopic redshifts lie within the DES area; this includes the 2SLAQ LRG sample (Cannon et al. 2006; Collister et al. 2007), with redshifts of red galaxies out to $z = 0.8$ that will be very useful for training cluster galaxy photo-z's. Likewise, the DES will overlap significantly with the 2dFGRS area, making another 90,000 spectroscopic redshifts available to DES at bright magnitudes $b_J < 19.45$.

At intermediate magnitudes, down to $r = 23$, U. Michigan DES collaborators are currently obtaining a large training set using the new, ultra-low dispersion prism, PRIMUS, combined with the IMACS multi-object spectrograph on the Magellan I telescope. This PRIMUS/IMACS survey can measure up to 15,000 redshifts per clear night, and a total sample of about 100,000 redshifts will be obtained to $r = 23$, selected from the deeper coadded imaging data available on SDSS Stripe 82. At the faintest magnitudes, down to the DES limit of $i \simeq 24$, we will use two ongoing deep redshift surveys: the VIMOS VLT Deep Survey (VVDS; Le Fevre et al. 2005) and the Keck DEEP2 Survey (Davis et al. 2004). The DES overlap areas with these surveys will provide about 60,000 VVDS redshifts down to $I_{AB} = 24$ and about 30,000 DEEP2 redshifts down to $R_{AB} = 24.1$. In addition, we will repeatedly image these redshift survey fields as part of the DES supernova survey, so that we will have very deep, well-calibrated photometric data for these faint training set galaxies.

We will carefully examine issues of sample completeness and fairness for these training sets, in order to identify any potential regions of redshift or galaxy parameter space with less certain photo-z's, so that we can use only well-understood photo-z galaxy samples in our science analyses. If necessary, we will also pursue additional spectroscopic programs to remedy any training set incompleteness at faint magnitudes, by

using the access of DES collaboration institutions to multi-object spectroscopic facilities available on large telescopes, including VLT, Magellan (as above), Gemini, and eventually LBT. Overall, the availability of some 350,000 spectroscopic redshifts before the start of DES observations will provide us with the necessary training sets to optimize our photo-z techniques, accurately characterize photo-z error distributions, and control our photo-z systematic errors so as not to compromise our cosmological parameter constraints.

8.2 Photo-z's for Clusters

The DES cluster key project requires accurate photo-z measurements for cluster galaxies, and such photo-z's are greatly facilitated by the strength of the 4000Å break feature prominently seen in the spectra of red cluster galaxies. Here use Monte Carlo simulations to assess the quality of DES cluster photo-z's. We adopt the local cluster luminosity function and luminosity-mass and number-mass relations of Lin, Mohr, & Stanford (2004), and use a passively evolving elliptical galaxy model from the Pegase-2 library (Fioc & Rocca-Volmerang 1997), for a flat cosmology with $\Omega_m = 0.3$ and $h = 0.7$. The cluster luminosity function faint-end slope is fixed at $\alpha = -1.1$, and we take the halo occupation number to evolve with redshift as $(1+z)^\gamma$, with $\gamma = 1$ (Lin, Mohr, & Stanford 2004; Kravtsov et al. 2004). We use the DES 10σ *griz* galaxy magnitude limits and add a 2% photometric calibration error in quadrature. A template fitting method is used to determine photo-z's for clusters with mass 1.0×10^{14} and $2.5 \times 10^{14} M_\odot$, and in each case 20,000 mock clusters are generated and distributed uniformly over the redshift range $z = 0 - 2$. Fig. 9 (left panel) shows our results and demonstrates that the DES will provide robust photo-z's for such clusters to $z \simeq 1.3$. For these clusters, we find a small photo-z scatter $\sigma(z) \simeq 0.02$ (68% limit), with the tails of the photo-z error distribution extending no more than about 0.05 in redshift. At higher redshifts, $z > 1.3$, color degeneracies become important, and the tails of the error distribution become larger, though the 68% limit scatter is still typically $\sigma(z) < 0.1$. (Note that our $\sigma(z)$ values are calculated from either the distribution or the rms of $z_{photometric} - z_{true}$, and we do **not** divide by a factor $1 + z_{true}$ as some other authors do.)

In addition, we have checked our cluster photo-z results using a sample of real clusters derived from the deeper coadded imaging data for the SDSS Stripe 82 area. In particular, using a set of nearly 5500 of these clusters which have spectroscopic redshifts for their brightest cluster galaxies, we find that we do indeed obtain photo-z errors $\sigma(z) = 0.01 - 0.02$ per cluster (68% limit), out to $z \simeq 0.6$, by averaging the photo-z's of individual cluster members; see Fig. 9 (right panel).

8.3 Photo-z's for Field Galaxies

The DES weak lensing, BAO/LSS, and supernova projects will also require photo-z measurements for the general field galaxy population. Such photo-z's are necessarily less accurate than those for cluster galaxies, as we must consider a much broader distribution of galaxy types. Nonetheless, our simulations show that the DES will obtain well-behaved photo-z's, with overall scatter $\sigma(z) < 0.1$ (68% limit) for redshifts $z < 2$ (Cunha et al. 2007). For our Monte Carlo simulations, we adopt the galaxy magnitude-redshift distribution derived from the luminosity functions of Lin et al. (1999) and Poli et al. (2003), combined with the galaxy type distribution derived using data in the GOODS/HDF-N field (Capak et al. 2004; Wirth et al. 2004; Cowie et al. 2004). We simulate a flux-limited sample of 100,000 galaxies, with redshifts $0 < z < 2$, magnitudes $20 < i < 24$, and compute photometric errors according to the DES 10σ *griz* magnitude limits. To optimize our photo-z's, we tested several different techniques, specifically polynomial fitting (e.g., Connolly et al. 1995), neural networks (e.g., Collister & Lahav 2004), and template fitting (Bolzonella et al. 2000; Benitez 2000). As shown in Fig. 10 (left), we find that our best results are derived from empirical training set methods, using either a neural network or a "nearest-neighbor polynomial" fitting technique, both of which give a photo-z scatter $\sigma(z) = 0.08$ (68% limit). We also find that we can derive well-behaved, nearly Gaussian-distributed photo-z errors using a "nearest-neighbor error" (NNE) estimator (Oyaizu et al. 2007), derived from the empirically measured photo-z error distribution of our training set galaxies.

We are testing our photo-z simulation results for their sensitivity to a variety of systematic effects. We are in the process of checking our results against details of the input mock galaxy catalogs, by using improved

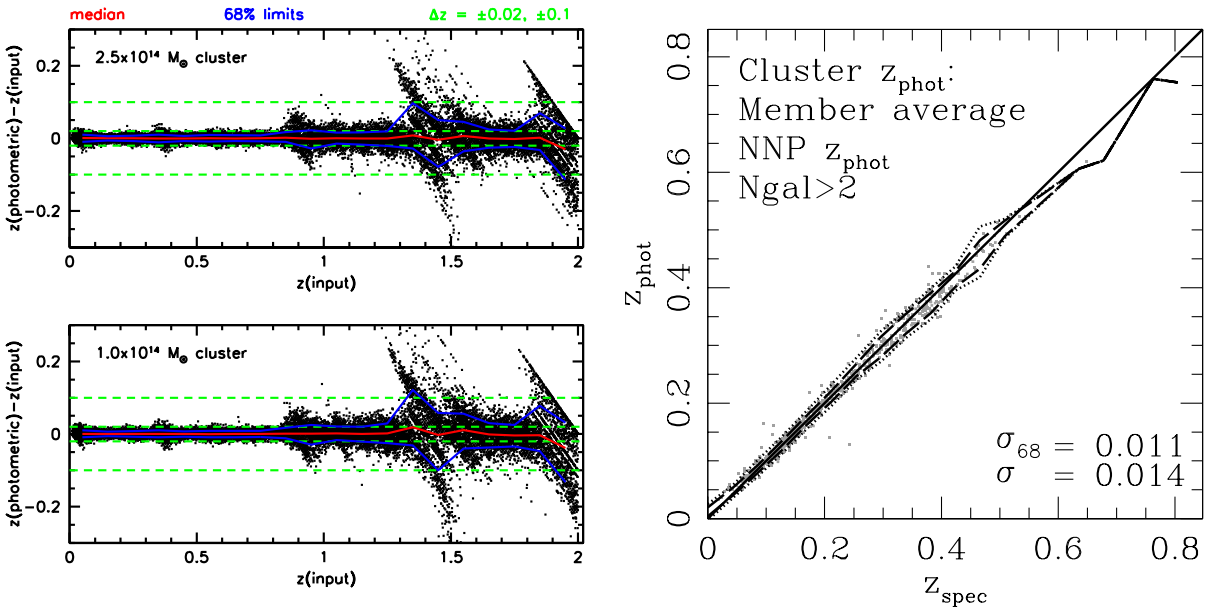

Figure 9: *Left:* Photo-z results for simulations of 1.0×10^{14} and $2.5 \times 10^{14} M_{\odot}$ galaxy clusters; see text for details. The red lines show the median difference between photometric and true redshift, the blue lines show the 68% limits, and the green lines are set at $\Delta z = \pm 0.02$ and ± 0.1 to guide the eye. *Right:* Photo-z results for a sample of real clusters derived from the coadded imaging data on SDSS Stripe 82. The nearest-neighbor polynomial (NNP) method was used, and cluster photo-z's were found by averaging the individual photo-z's of cluster members, demonstrating that we can obtain errors $\sigma(z) \simeq 0.01$ (68% limit) per cluster out to redshifts $z \simeq 0.6$ for real galaxy clusters.

catalogs drawn from large N-body simulations, as well as by varying the adopted input luminosity, redshift, type and reddening distributions to test for potential effects on the resulting photo-z errors. Moreover, we have also used real galaxy redshift survey samples with depths similar to DES, from which we find comparable photo-z errors as for our simulations. In addition, we are participating in the Blanco Cosmology Survey (PI: DES Collaborator J. Mohr), which is using the CTIO Mosaic-II camera to obtain 100 deg^2 of $griz$ imaging of similar depths as DES, including many of the same deep redshift survey fields that will be used for DES photo-z training. Finally, we have also verified that our fiducial choice of SDSS filter bandpass parameters is close to optimal, as demonstrated via a Markov Chain Monte Carlo study which optimized the photo-z scatter with respect to filter parameters, including central wavelengths and widths.

8.4 VISTA Near-IR Data

DES collaborators and others have submitted to ESO a proposal, the VISTA Hemisphere Survey (VHS; PI: DES collaborator R. McMahon), which will image 20,000 deg^2 of the southern celestial hemisphere using the VISTA telescope and near-IR camera. In particular, VHS will carry out deeper imaging over the 5000 deg^2 DES area in the J, H and K filters, with total exposure times of 120 sec per filter by the end of the first year of DES, and 240 sec per band by the end of the full DES. Very recently, the VHS proposal has been recommended for implementation by the VISTA Observing Programmes Committee. If the VHS proceeds as expected, we will enhance the synergy between DES and VISTA by using DECam to obtain Y-band imaging data over the DES area. Our current plan would be to obtain 400 sec Y-band exposures, while reducing the baseline 2000 sec z-band exposure time to 1600 sec, so that the enhanced $grizY$ survey will take the same time as the baseline $griz$ survey. Note that the $grizY$ survey still meets the DES galaxy photometric depth requirements, and we have verified that it has the same field and cluster galaxy photo-z

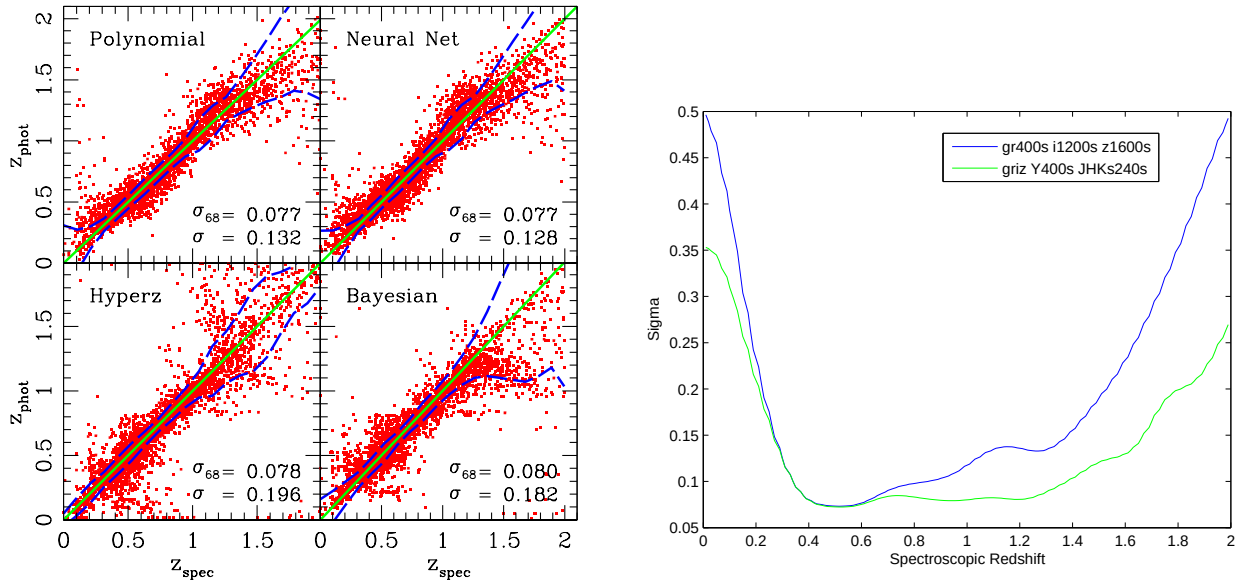

Figure 10: *Left:* $griz$ photo-z results for DES field galaxy simulations; see text for details. σ is the rms photo-z scatter, and σ_{68} indicates the 68% limits (blue lines). The panels show the results using different photo-z techniques; the nearest-neighbor polynomial and neural network methods perform the best. *Right:* σ vs. redshift for the baseline $griz$-only photo-z's and for the $grizYJHK$ photo-z's made possible by the addition of VISTA near-IR data (see text), which result in a factor of 2 improvement in σ over the $griz$-only photo-z's for the redshift range $1 < z < 2$.

quality as the $griz$ survey. The Y-band data will be combined with the VISTA JHK data to enhance DES science reach by enabling selection of cool stars and high-redshift quasars, and very importantly, we will use the resulting 8-band $grizYJHK$ optical plus near-IR data to improve DES galaxy photo-z's, in particular at redshifts $z \gtrsim 1$. Using the same field galaxy simulations described earlier, we show in Figure 10 (right) that we do in fact obtain significant photo-z improvement at high redshifts compared to using $griz$ data only, specifically a factor of two reduction in the overall photo-z scatter over the redshift range $z = 1 - 2$. Moreover, the addition of near-IR data will also significantly improve cluster photo-z's above a redshift $z \simeq 1.3$, a range which is difficult using optical $griz$ data alone (cf. Fig. 9 left panel).

8.5 Cross Talk with Science Key Projects

The limiting systematic error in degrading the cosmological parameter constraints is typically not the absolute size of any photo-z bias or scatter, but rather the uncertainty in knowing what that bias or scatter is (although BAO is an exception to this). Cosmology results could also suffer from the fraction of catastrophic outliers. We can divide the DES galaxy sample into photo-z bins and examine the effect on the cosmology constraints due to uncertainties in the photo-z bias and scatter in those bins (Ma, Hu, & Huterer 2006; Huterer et al. 2004). This is illustrated in Fig. 11 (Z. Ma, unpublished) for the weak lensing shear power spectrum (left panels) and for BAO (right panels). For example, to ensure $< 10\%$ degradation in the w_0 constraint from lensing tomography, we need to keep the photo-z bias uncertainty < 0.002 and the photo-z scatter uncertainty < 0.003 per redshift bin. Note that the same 10% degradation on the w_0 constraint from BAO requires only photo-z bias and scatter uncertainties at the ~ 0.01 level. A similar analysis for the cluster method indicates that we need an accuracy of about 0.005 in the cluster photo-z bias in bins of width $\Delta z = 0.1$. From Ma, Hu, & Huterer (2006), the photo-z bias uncertainty per redshift bin is given by $\sigma/\sqrt{N_{\rm spec}}$, where $N_{\rm spec}$ is the number of spectroscopic training set galaxies in that bin. Thus a bias

uncertainty requirement of 0.002 per bin, with a typical photo-z scatter $\sigma = 0.1$ per galaxy and 10 redshift bins, implies a required total training set size of 2.5×10^4 objects. The more detailed analysis of Ma, Hu, & Huterer (2006) shows that training sets of $10^4 - 10^5$ objects are needed in order to meet these requirements on the bias and scatter uncertainties. As indicated earlier, DES will satisfy this, as a sample of about 350,000 training set galaxies will be available.

Several ideas have been proposed recently to improve the performance of the weak lensing analysis. Jain, Connolly, & Takada (2007) suggested "color tomography" to bin the galaxy data in color space and to use the training sets accordingly, rather than to generate a photo-z catalog and then bin. Newman (2006) suggested that cross-correlation of a spectroscopic sample with a photometric sample could constrain the redshift distribution of the photometric sample, $n(z)$. Our team is actively testing these ideas and their extensions.

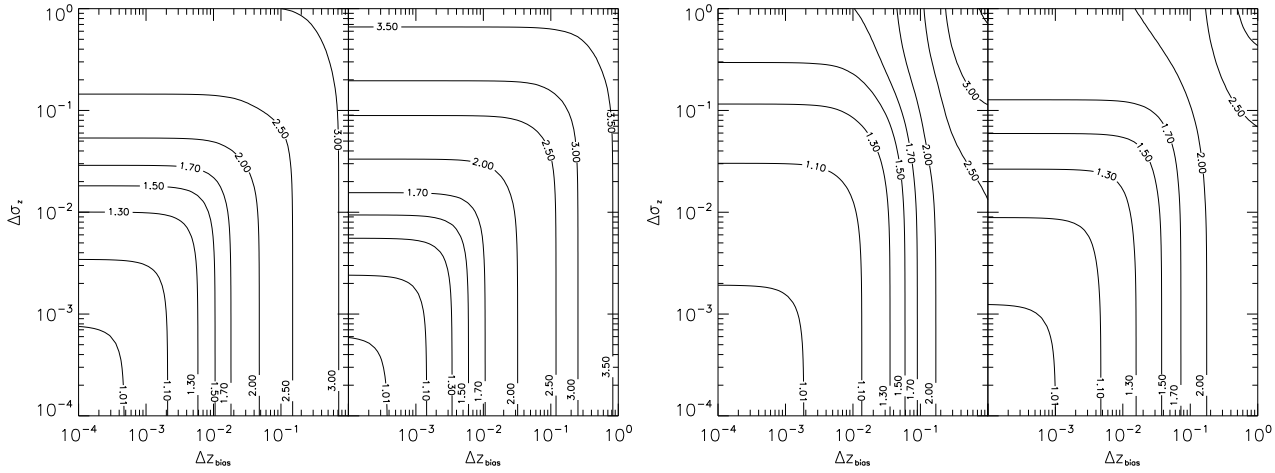

Figure 11: Contours of degradation in dark energy equation of state constraints derived from the WL shear power spectrum (left 2 panels) and from BAO (right 2 panels) as functions of the uncertainty (prior) in the photo-z bias (x-axis) and in the photo-z scatter (y-axis) in each redshift bin. Seven photo-z bins are used in the redshift range $z = 0 - 2$. The contour levels indicate the amount of degradation of the parameter constraints: w_0 in the left-hand panels of each pair, w_a in the right-hand panels. Note the constraint degradations are fairly modest ($\lesssim 1.5$) for photo-z bias and scatter uncertainties $\lesssim 0.01$.

References

Allen, S. W., Schmidt, R. W., Fabian, A. C., & Ebeling, H. 2003, MNRAS, 342, 287

Astier, P., et al. 2006, A&A, 447, 31

Bacon, D., Refregier, A., Clowe, D., & Ellis, R. 2000, MNRAS, 318, 625

Bahcall, N. A., et al. 2003, ApJ, 585, 182

Battye, R. A., & Weller, J. 2003, Phys. Rev. D, 68, 083506

Benitez, N. 2000, ApJ, 536, 571

Benson, B. A., et al. 2004, ApJ, 617, 829

Berlind, A., & Weinberg, D. H. 2002, ApJ, 575, 587

Bernardeau, F., Colombi, S., Gaztanaga, E., & Scoccimarro, R. 2002, Phys. Rept., 367, 1

Bernstein, G. & Jarvis, M. 2002, AJ, 123, 583

Bernstein, G. M., & Jain, B. 2003, ApJ, 600, 17

Blake, C. & Glazebrook, K., 2003, ApJ, 594, 665

Blake, C., Collister, A., Bridle, S., & Lahav, O. 2007, MNRAS, 374, 1527

Bolzonella, M., Miralles, J.-M., & Pello, R. 2000, A&A, 363, 476

Bond, J. R., et al. 2005, ApJ, 626, 12

Cabre, A., Gaztanaga, E., Manera, M., Fosalba, P., et al. 2006, MNRAS, 372, L23

Cabre, A., Fosalba, P., Gaztanaga, E., & Manera, M. 2007, MNRAS, 381, 1347

Cannon, R., et al. 2006, MNRAS, 372, 425

Capak, P., et al. 2004, AJ, 127, 180

Chae, K.-H. 2003, MNRAS, 346, 746

Cole, S., et al., 2005, MNRAS, 362, 505

Collister, A.A., & Lahav, O. 2004, PASP, 116, 345

Collister, A., et al. 2007, MNRAS, 375, 68

Connolly, A.J., et al. 1995, AJ, 110, 2655

Conroy, C., Wechsler, R. H., & Kravtsov, A. V. 2006, ApJ, 647, 201

Cooray, A., & Sheth, R. 2002, Physics Reports, 372, 1

Cowie, L.L., et al. 2004, AJ, 127, 3137

Crittenden, R. G., & Turok, N. 1996, Phys. Rev. Lett., 76, 575

Csabai, I., et al. 2003, AJ, 125, 580

Cunha, C., et al. 2007, in preparation

Dark Energy Survey Collaboration, T. Abbott et al. 2005, astro-ph/0510346 (DETF White Paper)

Davis, M., Gerke, B.F., & Newman, J.A. 2004, astro-ph/0408344, in *Observing Dark Energy*, ASP Conference Series, Vol. 339, eds. S. C. Wolff & T. R. Lauer (San Francisco: Astronomical Society of the Pacific), p.128

De Lucia, G., Springel, V., White, S. D. M., Croton, D., & Kauffmann, G., 2006, MNRAS, 366, 499

Dickinson, M., et al. 2004, ApJL, 600, L99

Dodelson, S., et al., 2002, ApJ, 572, 140

Dodelson, S. 2004, Phys. Rev. D, 70, 023008

Dolney, D., Jain, B., & Takada, M. 2006, MNRAS, 366, 884

Dressler, A., et al. 1997, ApJ, 490, 577

Eisenstein, D., et al., 2005, ApJ, 633, 560

Eisenstein, D., Seo H.-J., White M., 2007, ApJ, 664, 660

Evrard, A. E., et al. 2002, ApJ, 573, 7

Filippenko, A. V., & Sargent, W. L. W. 1989, ApJ, 345, L43

Fioc, M., & Rocca-Volmerange, B. 1997, A&A, 326, 950

Fosalba, P., Gaztanaga, E., & Castander, F. J. 2003, ApJ, 597, L89

Frieman, J., Huterer, D., Linder, E., & Turner, M. S. 2003, Phys. Rev. D, 67, 083505

Fryxell, B. et al. 2000, ApJS, 131, 273

Gaztanaga, E., Manera, M., & Multamaki, T. 2006, MNRAS, 365, 171

Giannantonio, T., et al. 2006, Phys. Rev. D, 74, 063520

Gladders, M. D., & Yee, H. K. C. 2000, AJ, 120, 2148

Gladders, M. D., & Yee, H. K. C. 2005, ApJS, 157, 1

Gladders, M. D., et al. 2007, ApJ, 655, 128

Golse, G., Kneib, J.-P., & Soucail, G. 2002, A & A, 387, 788

Guzik, J., Bernstein, G., & Smith, R. E. 2007, MNRAS, 375, 1329

Haiman, Z., Mohr, J., & Holder, G. P. 2001, ApJ, 553, 545

Hamuy, M., Phillips, M. M., Suntzeff, N. B., Schommer, R. A., Maza, J., & Aviles, R. 1996, AJ, 112, 2391

Hamuy, M., Trager, S. C., Pinto, P. A., Phillips, M. M., Schommer, Ivanov, V., & Suntzeff, N. B. 2000, AJ, 120, 1479

Hamuy, M, & Pinto, P. A. 2002, ApJ, 566, L63

Hansen, S. M., McKay, T. A., Wechsler, R. H., Annis, J., Sheldon, E. S., & Kimball, A. 2005, ApJ, 633, 122

Heitmann, K., Ricker, P. M., Warren, M. S., & Habib, S. 2005, ApJS, 160, 28

Hennawi, J. F., & Spergel, D. N. 2005, ApJ, 624, 59

Hennawi, J. F., et al. 2006, astro-ph/0610061

Heymans, C. et al., 2006, MNRAS, 371, 750

Hirata, C. & Seljak, U. 2003, MNRAS, 343, 459

Hoekstra, H., Yee, H., Gladders, M., 2002, ApJ, 577, 595

Hoekstra, H. et al., 2006, ApJ, 647, 116

Hu, W., 1999, ApJ, 522, L21

Hu, W. 2003, Phys. Rev. D, 67, 081304

Hu, W., & Jain, B. 2004, PRD, 70, 43009

Huterer, D., et al. 2004, ApJ, 615, 595

Huterer, D., Takada, M., Bernstein, G., & Jain, B., 2005, MNRAS, 366, 101

Huterer, D., & Takada, M. 2005, Astroparticle Phys., 23, 369

Huterer, D., & White, M. 2005, Phys. Rev. D, 72, 043002

Jain, B., & Taylor, A. 2003, Phys. Rev. Lett., 91, 141302

Jain, B., Jarvis, M., & Bernstein, G. 2006, JCAP, 0602, 001

Jain, B., Connolly, A., & Takada, M. 2007, JCAP, 03, 013

Jarvis, M., et al., 2003, AJ, 125, 1014

Jarvis, M., & Jain, B., 2004, ApJ, submitted, astro-ph/0412234

Jarvis, M., Jain, B., Bernstein, G., & Dolney, D. 2006, ApJ, 644, 71

Jenkins, A., Frenk, C. S., White, S. D. M., Colberg, J. M., Cole, S., Evrard, A. E., Couchman, H. M. P., & Yoshida, N. 2001, MNRAS, 321, 372

Jha, S., et al. 2006, AJ, 131, 527

Jing, Y. P., Zhang, P., Lin, W. P., Gao, L., & Springel, V. 2006, ApJ, 640, L119

Johnston, D. E., Sheldon, E. S., Tasitsiomi, A., Frieman, J. A., Wechsler, R., & McKay, T. A. 2005, ApJ, 656, 27

Johnston, D. E., Sheldon, E. S., Wechsler, R. H., Rozo, E., Koester, B. P., Frieman, J. A., McKay, T. A., Evrard, A. E., Becker, M. R., Annis, J. 2007, astro-ph/0709.1159

Kaiser, N., 1992, ApJ, 388, 272

Kaiser, N., Wilson, G., & Luppino, G., 2000, astro-ph/0003338

Kim, A. G., & Miquel, R. 2006, Astropart. Phys. 24, 451

Koester, B., et al., 2007, ApJ, 660, 239

Kravtsov, A. V. 1999, PhD thesis

Kravtsov, A. V., Klypin, A., & Hoffman, Y. 2002, ApJ, 571, 563

Kravtsov, A. V., et al. 2004, ApJ, 609, 35

Kravtsov, A. V., Vikhlinin, A., & Nagai, D. 2006, ApJ, 650, 128

Kuhlen, M., Keeton, C. R., & Madau, P. 2004, ApJ, 601, 104

Kuo, C. L., et al. 2007, ApJ, 664, 687

Le Fevre, O., et al. 2005, A&A, 439, 845

Lewis, G. F., & Ibata, R. A. 2002, MNRAS, 337, 26

Lima, M., & Hu, W. 2004, Phys. Rev. D, 70, 043504

Lima, M., & Hu, W. 2005, Phys. Rev. D, 72, 043006

Lin, H., et al. 1999, ApJ, 518, 533

Lin, Y.-T., Mohr, J. J., & Stanford, S.A. 2003, ApJ, 591, 749

Lin, Y.-T., Mohr, J. J., & Stanford, S.A. 2004, ApJ, 610, 745

Lin, Y.-T., & Mohr, J. J. 2007, ApJS, 170, 71

Lin, W. P., Jing, Y. P., Mao, S., Gao, L., & McCarthy, I. G. 2006, ApJ, 651, 636

Linder, E., 2003, Phys. Rev. D, 68, 083504.

Linder, E. 2004, Phys. Rev. D, 70, 043534

Link, R., & Pierce, M. J. 1998, ApJ, 502, 63

LoVerde, M., Hui, L., & Gaztanaga, E. 2007, Phys. Rev. D, 75, 043519

Ma, Z., Hu, W., & Huterer, D. 2006, ApJ, 636, 21

Majumdar, S., & Mohr, J. J. 2003, ApJ, 585, 603

Majumdar, S., & Mohr, J. J. 2004, ApJ, 613, 41

Mandelbaum, R., Hirata, C. M., Ishak, M., Seljak, U., & Brinkmann, J. 2006, MNRAS, 367, 611

Massey, R. *et al.*, 2007, MNRAS, 376, 13

Melin, J.-B., Bartlett, J. G., & Delabrouille, J. 2005, Astron. Astrophys., 429, 417

Metzler, C. A., White, M., & Loken, C. 2001, ApJ, 547, 560

Nagai, D. 2006, ApJ, 650, 538

Nagai, D., Vikhlinin, A., & Kravtsov, A. V. 2007, ApJ, 655, 98

Nakajima, R., & Bernstein, G. 2007, AJ, 133, 1763

Neill, J. D., et al. 2006, AJ, 132, 1126

Newman, J.A. 2006, unpublished

Nugent, P. et al. 2006, ApJ, 645, 841

O'Hara, T. B., Mohr, J. J., Bialek, J. J., & Evrard, A. E. 2006, ApJ, 639, 64

Oyaizu, H., Lima, M., Cunha, C., Lin, H., & Frieman, J. 2007, astro-ph/0711.0962

Padmanabhan, N., et al. 2007, MNRAS, 378, 852

Percival, W., et al., 2007a, ApJ, 657, 51

Percival, W., et al., 2007b, ApJ, 657, 645

Perlmutter, S., et al. 1999, ApJ, 517, 565

Phillips, M. M. 1993, ApJ, 413, L105

Pogosian, L., et al. 2005, Phys. Rev. D, 72, 103519

Poli, F., et al. 2003, ApJ, 593, L1

Randall, S., Sarazin, C., & Ricker, P. M. 2002, ApJ, 577, 579

Reed, D., Bower, R., Frenk, C. Jenkins, A., & Theuns, T. 2007, MNRAS, 374, 2

Riess, A. G., et al. 1998, AJ, 123, 745

Riess, A. G., et al. 1999, AJ, 117, 707

Riess, A. G., et al. 2007, ApJ, 659, 98

Ruhl, J. E., et al. 2004, astro-ph/0411122, in Proc. SPIE, 5498, 11

Sawicki, M.J., Lin, H., & Yee, H.K.C 1997, AJ, 113, 1

Schulz, A. E., & White, M. 2003, ApJ, 586, 723

Scranton, R., et al. 2003, astro-ph/0307335

Sealfon, C., Verde, L., & Jimenez, R. 2006, ApJ, 649, 118

Sefusatti, E., & Scoccimarro, R., 2005, Phys. Rev. D, 71, 063001

Sefusatti, E., Crocce, M., Pueblas, S., & Scoccimarro, R. 2006, Phys. Rev. D, 74, 023522

Seljak, U., Sugiyama, N., White, M., & Zaldarriaga, M. 2003, Phys. Rev. D, 68, 3507

Seljak, U., & Warren, M. S., 2004, MNRAS, 355, 129

Seljak, U., et al. 2005, Phys. Rev. D, 71, 103515

Semboloni, E., et al. 2006, A & A, 452, 51

Seo, H.-J., & Eisenstein, D. J., 2003, ApJ, 598, 720

Seo, H.-J., & Eisenstein, D. J. 2005, ApJ, 633, 575

Sheldon, E. S., Johnston, D. E., Frieman, J. A., Scranton, R., McKay, T. A., Connolly, A. J., Budavari, T., Zehavi, I., Brinkmann, J., & Fukugita, M. 2004, AJ, 127, 2544

Sheldon, E. S., Johnston, D. E., Scranton, R., Koester, B. P., McKay, T. A., Oyaizu, H., Cunha, C., Lima, M., Lin, H., Frieman, J. A., Wechsler, R. H., Annis, J., Mandelbaum, R., Bahcall, N. A., Fukugita, M., astro-ph/0709.1153

Smith, R., et al. 2003, MNRAS, 341, 1311

Smith, R., Scoccimarro, R., & Sheth, R., 2007, Phys. Rev. D, 75, 063512

Song, Y.-S. 2005, Phys. Rev. D, 71, 024026

Spergel, D., et al. 2007, ApJS, 170, 377

Springel, V., et al., 2005, Nature, 435, 629

Sullivan, M., et al. 2003, MNRAS, 340, 1057

Sullivan, M., et al. 2006, ApJ, 648, 868

Sunyaev, R. A., & Zel'dovich, Y. B. 1970, Comm. Astrophys. & Space Phys., 2, 66

Takada, M., & Jain, B., 2004, MNRAS, 348, 897

Tegmark, M., et al., 2002, ApJ, 571, 191

Tegmark, M., et al., 2006, Phys. Rev. D, 74, 123507

Vale, C., & White, M. 2006, New Astronomy, 11, 207

Van Waerbeke, L., Mellier, Y., Erben, T., Cuillandre, J. C., Bernardeau, F., Maoli, R., Bertin, E., McCracken, H. J., Le Fevre, O., Fort, B., Dantel-Forti, M., Jain, B., & Schneider, P. 2000, A&A, 358, 30

Wang, L., & Steinhardt, P. J. 1998, ApJ, 508, 483

Warren, M. S., Abazajian, K., Holz, D. E., & Teodoro, L. 2006, ApJ, 646, 881

Wechsler, R., et al. 2007, in preparation

White, M. 2004, Astroparticle Physics, 22, 211

White, M., & Majumdar, S. 2004, ApJ, 602, 565

White, M., 2005, Astroparticle Physics, 24, 334

Wirth, G.D., et al. 2004, AJ, 127, 3121

Wittman, D. M., Tyson, A. J., Kirkman, D., Dell'Antonio, I., & Bernstein, G., 2000, Nature 405, 143

Wittman, D., Dell'Antonio, I. P., Hughes, J. P., Margoniner, V. E., Tyson, J. A., Cohen, J. G., & Norman, D. 2006, ApJ, 643, 128

Yee, H. K. C., & Ellingson, E. 2003, ApJ, 585, 215

Yoo, J., Tinker, J. L., Weinberg, D. H., Zheng, Z., Katz, N., & Davé, R. 2006, ApJ, 652, 26

York, D. G., et al. 2000, AJ, 120, 1579

Zhan, H., & Knox, L. 2004, ApJL, 616, L75

Zhang, J., Hui, L., & Stebbins, A. 2005, ApJ, 635, 806